

OPEN ACCESS

The ATLAS TRT end-cap detectors

To cite this article: The ATLAS TRT collaboration *et al* 2008 *JINST* **3** P10003

View the [article online](#) for updates and enhancements.

Related content

- [The ATLAS TRT Barrel Detector](#)
The ATLAS TRT collaboration, E Abat, T N Addy *et al.*
- [Engineering for the ATLAS SemiConductor Tracker \(SCT\) End-cap](#)
A Abdesselam, P P Allport, B Anderson *et al.*
- [Alignment of the ATLAS inner detector tracking system](#)
Daniel Kollár and the Atlas Collaboration

Recent citations

- [Performance of the ATLAS Transition Radiation Tracker in Run 1 of the LHC: tracker properties](#)
M. Aaboud *et al*
- [Gas gain stabilisation in the ATLAS TRT detector](#)
B. Mindur *et al*
- [Operations and performance of the CMS RPC muon system at LHC](#)
Anna Cimmino

RECEIVED: July 21, 2008

REVISED: September 11, 2008

ACCEPTED: October 7, 2008

PUBLISHED: October 21, 2008

The ATLAS TRT end-cap detectors

The ATLAS TRT collaboration

E. Abat,^{a,†} T.N. Addy,^j T.P.A. Åkesson,^m J. Alison,^u F. Anghinolfi,^c E. Arik,^{a,†} M. Arik,^a G. Atoian,^z B. Auerbach,^z O.K. Baker,^z E. Banas,^f S. Baron,^c C. Bault,^c N. Becerici,^a A. Beddall,^{a,1} A.J. Beddall,^{a,1} J. Bendotti,^c D.P. Benjamin,^g H. Bertelsen,^d A. Bingul,^{a,1} H. Blampey,^c A. Bocci,^g M. Bochenek,^e V.G. Bondarenko,^p V. Bychkov,^l J. Callahan,^k M. Capeáns Garrido,^c L. Cardiel Sas,^c A. Catinaccio,^c S.A. Cetin,^{a,2} T. Chandler,^z R. Chritin,^h P. Cwetanski,^k M. Dam,^d H. Danielsson,^c E. Danilevich,^v E. David,^c J. Degenhardt,^u B. Di Girolamo,^c F. Dittus,^c N. Dixon,^c D. Dobos,^c O.B. Dogan,^{a,†} B.A. Dolgoshein,^p N. Dressnandt,^u C. Driouchi,^d W.L. Ebenstein,^g P. Eerola,^m U. Egede,^m K. Egorov,^k H. Evans,^k P. Farthouat,^c O.L. Fedin,^{v*} A.J. Fowler,^g S. Fratina,^u D. Froidevaux,^c A. Fry,^j P. Gagnon,^k I.L. Gavrilenco,^o C. Gay,^y N. Ghodbane,^r J. Godlewski,^c M. Goulette,^c I. Gousakov,^l N. Grigalashvili,^l Y. Grishkevich,^q J. Grognuz,^c Z. Hajduk,^f M. Hance,^u F. Hansen,^d J.B. Hansen,^d J.D. Hansen,^d P.H. Hansen,^d G.A. Hare,^u A. Harvey Jr.,^j C. Hauviller,^c A. High,^u W. Hulsbergen,^c W. Huta,^c V. Issakov,^z S. Istin,^a V. Jain,^k G. Jarlskog,^m L. Jeanty,^y V.A. Kantserov,^p B. Kaplan,^z A.S. Kapliy,^u S. Katounine,^v F. Kayumov,^o P.T. Keener,^u G.D. Kekelidze,^l E. Khabarova,^l A. Khristachev,^v B. Kisielewski,^f T.H. Kittelmann,^w C. Kline,^k E.B. Klinkby,^d N.V. Klopov,^v B.R. Ko,^g T. Koffas,^c N.V. Kondratieva,^p S.P. Konovalov,^o S. Koperny,^e H. Korsmo,^m S. Kovalenko,^v T.Z. Kowalski,^e K. Krüger,^c V. Kramarenko,^q L.G. Kudin,^v A-C. Le Bihan,^c B.C. LeGeyt,^u K. Levterov,^l P. Lichard,^c A. Lindahl,^d V. Lisan,^l S. Lobastov,^l A. Loginov,^z C.W. Loh,^y S. Lokwitz,^z M.C. Long,^j S. Lucas,^c A. Lucotte,ⁱ F. Luehring,^k B. Lundberg,^m R. Mackeprang,^d V.P. Maleev,^v A. Manara,^k M. Mandl,^c A.J. Martin,^z F.F. Martin,^u R. Mashinistov,^p G.M. Mayers,^u K.W. McFarlane,^j V. Mialkovski,^l B.M. Mills,^y B. Mindur,^e V.A. Mitsou,^x J.U. Mjörnmark,^m S.V. Morozov,^p E. Morris,^k S.V. Mouraviev,^o A.M. Muir,^y A. Munar,^u A.V. Nadtochi,^v S.Y. Nesterov,^v F.M. Newcomer,^u N. Nikitin,^q O. Novgorodova,^o E.G. Novodvorski,^v H. Ogren,^k S.H. Oh,^g S.B. Oleshko,^v D. Olivito,^u J. Olszowska,^f W. Ostrowicz,^f M.S. Passmore,^c S. Patrichev,^v J. Penwell,^k F. Perez-Gomez,^c V.D. Peshekhonov,^l T.C. Petersen,^c R. Petti,^b A. Placci,^c A. Poblaquev,^z X. Pons,^c M.J. Price,^c O. Røhne,^t R.D. Reece,^u M.B. Reilly,^u C. Rembser,^c A. Romanouk,^p D. Rousseau,^s D. Rust,^k Y.F. Ryabov,^v V. Ryjov,^c M. Söderberg,^m A. Savenkov,^l J. Saxon,^u M. Scandurra,^k V.A. Schegelsky,^v M.I. Scherzer,^u M.P. Schmidt,^{z,†}

2008 JINST 3 P10003

C. Schmitt,^c E. Sedykh,^v D.M. Seliverstov,^v T. Shin,^j A. Shmeleva,^o S. Sivoklokov,^q S.Yu. Smirnov,^p L. Smirnova,^q O. Smirnova,^m P. Smith,^k V.V. Sosnovtsev,^p G. Sprachmann,^c S. Subramania,^k S.I. Suchkov,^p V.V. Sulin,^o R.R. Szczygiel,^f G. Tartarelli,ⁿ E. Thomson,^u V.O. Tikhomirov,^o P. Tipton,^z J.A. Valls Ferrer,^x R. Van Berg,^u V.I. Vassilakopoulos,^j L. Vassilieva,^o P. Wagner,^u R. Wall,^z C. Wang,^g D. Whittington,^k H.H. Williams,^u A. Zhelezko^p and K. Zhukov^o

^a*Faculty of Sciences, Department of Physics, Bogazici University,
TR - 80815 Bebek-Istanbul, Turkey*

^b*Brookhaven National Laboratory, Physics Department,
Bldg. 510A, Upton, NY 11973, United States of America*

^c*CERN, CH - 1211 Geneva 23, Switzerland, Switzerland*

^d*Niels Bohr Institute, University of Copenhagen,
Blegdamsvej 17, DK - 2100 Kobenhavn 0, Denmark*

^e*Faculty of Physics and Applied Computer Science of the AGH-University of Science and
Technology, (FPACS, AGH-UST), al. Mickiewicza 30, PL-30059 Cracow, Poland*

^f*The Henryk Niewodniczanski Institute of Nuclear Physics, Polish Academy of Sciences, ul.
Radzikowskiego 152, PL - 31342 Krakow, Poland*

^g*Duke University, Department of Physics, Durham, NC 27708, United States of America*

^h*Universite de Geneve, Section de Physique,
24 rue Ernest Ansermet, CH - 1211 Geneve 4, Switzerland*

ⁱ*Laboratoire de Physique Subatomique et de Cosmologie, CNRS-IN2P3, Universite Joseph
Fourier, INPG, 53 avenue des Martyrs, FR - 38026 Grenoble Cedex, France*

^j*Hampton University, Department of Physics, Hampton, VA 23668, United States of America*

^k*Indiana University, Department of Physics, Swain Hall West, Room 117, 727 East Third St.,
Bloomington, IN 47405-7105, United States of America*

^l*Joint Institute for Nuclear Research, JINR Dubna, RU - 141 980 Moscow Region, Russia*

^m*Lunds Universitet, Fysiska Institutionen, Box 118, SE - 221 00 Lund, Sweden*

ⁿ*INFN Milano and Università di Milano, Dipartimento di Fisica,
via Celoria 16, IT - 20133 Milano, Italy*

^o*P.N. Lebedev Institute of Physics, Academy of Sciences,
Leninsky pr. 53, RU - 117 924 Moscow, Russia*

^p*Moscow Engineering & Physics Institute (MEPhI),
Kashirskoe Shosse 31, RU - 115409 Moscow, Russia*

^q*Lomonosov Moscow State University, Skobeltsyn Institute of Nuclear Physics,
RU - 119 992 Moscow Leninskies gory 1, Russia*

^r*Max Planck Institut fuer Physik,
Postfach 401212, Foehringer Ring 6, DE - 80805 Muenchen, Germany*

^s*LAL, Univ. Paris-Sud, IN2P3/CNRS, Orsay, France*

^t*Department of Physics, University of Oslo, Blindern, NO - 0316 Oslo 3, Norway*

^u*University of Pennsylvania, Department of Physics & Astronomy,
209 S. 33rd Street, Philadelphia, PA 19104, United States of America*

^v*Petersburg Nuclear Physics Institute, RU - 188 300 Gatchina, Russia*

^w*University of Pittsburgh, Department of Physics and Astronomy,
3941 O'Hara Street, Pittsburgh, PA 15260, United States of America*

^x*Instituto de Física Corpuscular (IFIC), Centro Mixto UVEG-CSIC, Apdo. 22085, ES-46071
Valencia; Dept. Física At., Mol. y Nuclear, Univ. of Valencia and Instituto de Microelectrónica
de Barcelona (IMB-CNM-CSIC), 08193 Bellaterra, Barcelona, Spain*

^y*University of British Columbia, Dept of Physics,
6224 Agricultural Road, CA - Vancouver, B.C. V6T 1Z1, Canada*
^z*Yale University, Department of Physics,
PO Box 208121, New Haven CT, 06520-8121, United States of America*
¹*Currently at Gaziantep University, Turkey*
²*Currently at Dogus University, Istanbul*
[†]*Deceased*
E-mail: Oleg.Fedin@cern.ch

ABSTRACT: The ATLAS TRT end-cap is a tracking drift chamber using 245,760 individual tubular drift tubes. It is a part of the TRT tracker which consist of the barrel and two end-caps. The TRT end-caps cover the forward and backward pseudo-rapidity region $1.0 < |\eta| < 2.0$, while the TRT barrel central η region $|\eta| < 1.0$. The TRT system provides a combination of continuous tracking with many measurements in individual drift tubes (or straws) and of electron identification based on transition radiation from fibers or foils interleaved between the straws themselves. Along with other two sub-systems, namely the Pixel detector and Semi Conductor Tracker (SCT), the TRT constitutes the ATLAS Inner Detector. This paper describes the recently completed and installed TRT end-cap detectors, their design, assembly, integration and the acceptance tests applied during the construction.

KEYWORDS: Particle tracking detectors; Transition radiation detectors; Large detector systems for particle and astroparticle physics.

*Corresponding author.

Contents

1. Introduction	2
2. The basic detector unit: the eight plane wheel	4
2.1 Design of an eight plane wheel	5
3. Description of the eight plane wheel components	8
3.1 The carbon fiber rings	8
3.2 The detecting elements: straws-preparation and quality control	10
3.2.1 Straw reinforcement	10
3.2.2 Straw production and quality control	12
3.3 Connecting and insulating straws: high voltage plugs, insulation end plugs and crimp pins	14
3.3.1 High voltage plugs	14
3.3.2 Insulation end plugs	15
3.3.3 Crimp pins	16
3.3.4 High voltage sleeves	16
3.4 The Wheel End-Cap Board (WEB)	17
3.4.1 Quality assurance for the WEBs	19
3.5 The radiators	21
3.5.1 Selection of materials	21
3.5.2 Radiator types and dimensions	22
3.5.3 Assembly and quality control of the radiators	23
3.6 Sealing the active gas volume: carters, cavaliers and passive WEBs	24
3.7 Aging studies	25
4. Assembly of eight plane wheel	25
4.1 The basic assembly unit: the four plane wheel	26
4.1.1 Assembly of the four plane wheels structure: rings, straws and radiators	26
4.1.2 Gas tightness test of the four plane wheel structure	27
4.1.3 Glueing of the Wheel End-Cap Boards	28
4.1.4 High voltage connection and insertion of wires	29
4.1.5 Sealing of the active gas volume: assembly of third ring, passive WEBs and carters	31
4.2 Combining two four plane wheels to an eight plane wheel	32
4.2.1 Quality control and wheel passport	33
4.3 Eight plane wheels acceptance tests at CERN	33
4.3.1 Measurement of wheel dimensions	33
4.3.2 Measurement of wire tension	34
4.3.3 Measurement of wheel gas tightness	35

4.3.4 Long term high voltage test	36
4.3.5 Straw straightness measurement	36
5. The end-cap group	43
5.1 Overview on the design of an end-cap group	43
5.2 Assembly and integration	43
5.2.1 Mechanical assembly	43
5.2.2 Mounting and testing of the on-detector electronics	46
5.2.3 Mounting and testing of monitoring sensors	49
6. Services	50
6.1 Distribution of active gas	50
6.2 Electronics cooling	51
6.3 Straw cooling	52
6.3.1 Requirements	52
6.3.2 System tests and validation	52
6.3.3 The pump module	53
6.3.4 The gas renewal module	53
6.3.5 The distribution racks	54
6.3.6 Installation on detector and control racks	54
7. Summary of weights and material distribution	55
8. Performance of end-cap modules at beam tests	56
9. Summary and conclusion	58
A. Summary of acceptance tests	59
B. Fact sheet	62

1. Introduction

The Transition Radiation Tracker (TRT) is one of the three subsystems of the ATLAS central tracker, the Inner Detector [1, 2]. It is designed to operate in a 2 T solenoidal magnetic field and to provide a solid tracking information and particle identification at the design luminosity $L = 10^{34} \text{ cm}^2\text{s}^{-1}$ of the Large Hadron Collider (LHC) with up to 22 overlaying proton collisions in a single bunch crossing of the proton beams each 25 ns. A view of one quadrant of the Inner Detector is shown in figure 1. The three detector technologies are indicated, starting with a Silicon Pixel Detector [3] close to the primary interaction point for identifying secondary vertices, e.g. to tag heavy quarks, then a Semi Conductor Tracker (SCT) [4, 5] for a precise measurement of

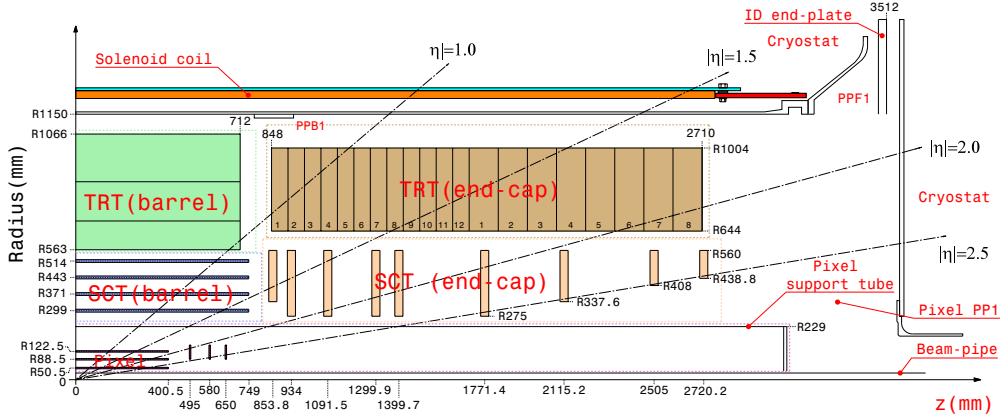


Figure 1. Plan view of a quarter-section of the ATLAS inner detector showing each of the major detector elements with its active dimensions and envelopes. The end-cap TRT spans the region from $827 < |z| < 2744$ mm and $617 < R < 1106$ mm in this view, covering a pseudo-rapidity (η) range of $1.0 < |\eta| < 2.0$.

the tracks transverse momentum perpendicular to the incoming particle beams and finally the TRT occupying the outer region of the cryostat bore.

The TRT section of the tracker is formed from a central TRT barrel Detector [6] with sensor layers parallel to the beam axis¹ and two (forward and backward) TRT end-caps with their sensor layers radial to the beam axis. The TRT end-caps cover the forward and backward η region $1.0 < |\eta| < 2.0$. The full length of each end-cap is 1.9 meter, the diameter is about 2.2 meter and the weight is about 1119 kg.

The TRT end-caps provide both continuous tracking in individual axial drift tubes (or straws) and electron identification using the straws to absorb and to detect transition radiation X-ray photons originating from thin foils between the straw layers. The requirement for the momentum measurement is to contribute to the overall tracking performance by providing a measurement in the $R\text{-}\varphi$ plane to reach $30 \mu\text{m}$ at luminosity of $L = 10^{33} \text{ cm}^2\text{s}^{-1}$ and $50 \mu\text{m}$ at $L = 10^{34} \text{ cm}^2\text{s}^{-1}$ [7]. The particle identification is designed to identify clean samples of electrons covering a wide range of particle momenta with a p_T between 20 GeV and 40 GeV reaching a rejection factor for charged pions of about 10. The expected number of transition radiation (TR) photons depends on the length of the track inside the TRT, e.g. for an electron with a momentum of 40 GeV about 11 TR photons are expected at $|\eta| \sim 1.7$ and 5 TR photons for an electron passing the detector at $|\eta| \sim 2.0$. On average about eight transition radiation (TR) photons are expected for an electron at 40 GeV.

This paper gives an overview of the design, construction and assembly of the TRT end-cap detectors and it is organised as follows. In section 2, the design of the basic detector unit, the so-called eight plane wheel is discussed. Section 3 lists all elements of the eight plane wheel and

¹The ATLAS coordinate system is a right-handed system in which the beam direction defines the z -axis and the $x\text{-}y$ plane is transverse to the beam direction. The positive x -axis is defined as pointing from the interaction point to the centre of the LHC ring and the positive y axis is defined as pointing upwards. The side-A of the ATLAS detector is defined as that with the positive z and side-C is that with negative z . The azimuthal angle φ is measured around the beam axis, and the polar angle θ is the angle from the beam axis. The pseudo-rapidity is defined as $\eta \equiv -\ln(\tan(\frac{\theta}{2}))$. The transverse momentum p_T is defined as the momentum of a particle in the $x\text{-}y$ plane. A position of any point in the $x\text{-}y$ plane is described by the radius $R = \sqrt{x^2 + y^2}$ and the azimuthal angle φ .

describes their design, production, assembly and quality control in detail. In section 4 the assembly steps of an eight plane wheel are described. Section 5 summarises the stacking and merging of a number of eight plane wheels to a complete end-cap group and the mounting of the on-detector electronics plus the control and monitoring sensors. In section 6 the various service installations to supply the detector with active gas, to cool its electronics and cool the detecting elements are described. Sections 7 and 8 summarise the material distribution and weight of the end-cap detector as built and give a brief overview of the performance test of end-cap modules in various beam tests.

2. The basic detector unit: the eight plane wheel

The TRT end-cap design follows the general features characteristic of any tracking system in a collider experiment of which the most essential is the minimization of the dead area for high momentum particles. Each end-cap has a total of 122,880 drift tubes (or straws) with a fairly uniform occupancy.

The straws form a uniform array in the azimuthal plane perpendicular to the beam axis, with a spacing of about $\frac{360^\circ}{768}$ between centers in the φ -plane and 8 mm or 15 mm in the z direction. The layout of the straws was designed to optimize the probability of the detection of transition radiation as well as to maximize the number of hits along a track. The straw diameter was chosen to be 4 mm as a reasonable compromise between speed of response, number of ionization clusters, and mechanical and operational stability. The straw anode is 31 μm -diameter gold-plated tungsten wire at ground potential and the cathode is the straw wall. The straw is typically operated at a high voltage of -1530 V, corresponding to a gas gain 2.5×10^4 for the gas mixture 70% Xe, 27% CO₂, and 3% O₂.

The mechanical design of the TRT end-caps must provide high mechanical rigidity and dimensional stability with a minimum amount of material and weight. For reasons of efficient construction, handling, testing and transportation, the end-caps are not built as a single mechanical structure but each end-cap is built up from two types of identical independent modules. The modular design approach reduces risk during assembly, enables distributed production at several assembly sites and sped up the final assembly process because each module could be tested independently.

Along the z-axis in each TRT end-cap there is a total of 160 layers of straws, each layer containing 768 individual straws. The straws are arranged so that every charged particle with a transverse momentum $p_T > 0.5 \text{ GeV}$ and with a pseudo-rapidity η between $1.0 < |\eta| < 2.0$ produces hits in 20 to 36 straws and so that the track can be measured with an intrinsic accuracy of $\sim 30\text{-}50 \mu\text{m}$. Each end-cap detector has a total of 122,880 straw tubes and matching electronics channels.

The independent modules that make up the TRT end-caps are referred to as wheels because of their cylindrical form and radial straws like spokes. Each mechanically independent wheel contains eight planes of straws but the two types, A-type and B-type differ in the z spacing of these planes. In both cases each of these layers contains 768 radially oriented straws of $\sim 37 \text{ cm}$ length with uniform azimuthal spacing but stepped, layer to layer, in φ .

In the first type, the so-called A-type wheels which make up the 96 straw layers closest to the interaction point, adjacent straw planes have a clearance of 4 mm in the z-direction. The B-type wheels which make up the remaining 64 layers have a clearance of 11 mm so that tracks at small

Table 1. TRT end-cap parameters. The minimum (maximum) pseudo-rapidity $|\eta_{\min}|$ ($|\eta_{\max}|$) corresponds to the maximum (minimum) end-cap radius $R_{\max}=1004$ mm ($R_{\min}=644$ mm) at minimum (maximum) position of the end-cap along z-axis z_{\min} (z_{\max}).

Wheel type	Number of eight plane wheels	Layers	Straws	$ \eta_{\min} $	$ \eta_{\max} $	z_{\min} (mm)	z_{\max} (mm)	Mass (kg)
A	12	96	73,728	0.77	1.7	848	1710	424
B	8	64	49,152	1.32	2.0	1740	2710	438
Total for end-cap	20	160	122,880					862

θ angles cross approximately the same number of straws as tracks at larger angles. The space between successive straw layers in each wheel is filled with layers of 15 μm thick polypropylene radiator foils separated by a polypropylene net.

The number of straws and the coverage in η and z for each set of wheels is listed in table 1. The mass listed in the table is for wheels, with electronics but without external services connected. The total weight of an end-cap including the connected services is ~ 1119 kg [8].

2.1 Design of an eight plane wheel

A cross-section of an eight plane wheel is shown in figure 2. Each eight-plane wheel is assembled from two back-to-back four-plane assembly units or four-plane wheels which contain four layers of radial straws.

The design of the present TRT end-cap is based on experience gained from an earlier design that was developed in the framework of LHC detector R&D (RD6) [9]. In this first design, the basic module had 16 planes. The main experience gained during the R&D programme was that a 16-plane module was too large and that the modularity should be determined by ease of manufacture and the ability to test for such aspects as leak-tightness, electrical viability and dimensional integrity at every stage of the construction. For this reason, in the final design, a four-plane module was chosen as the basic construction unit. In itself a four-plane module is a mechanically stable unit, but it is only when two of these four-plane modules are combined to make an eight-plane wheel that an autonomous device (from the point of view of electronics and active gas distribution) is obtained.

The fundamental support elements in the four-plane module are three concentric carbon-fibre reinforced rings. These rings are numbered consecutively with ring 1 the innermost. Rings 1 and 2 are drilled with holes to accept the straws. Ring 3 is solid. The outer structure of the four-plane module has the form of a reinforced beam, consisting of ring 2 and ring 3 linked by lateral elements, so called Wheel End-Cap Boards (see figure 2), connected by 'spokes' (carbon fibre reinforced straws) to an inner 'hub' (ring 1 made gas-tight by a Kapton® casing). One of the major design concerns was to make the structure strong enough to reduce the deformations to the order of a few tenths of a millimetre under the module's own weight.

To assemble a four plane wheel, straws were inserted and glued into precisely drilled holes in the inner and outer carbon-fiber rings or C-fiber ring. They are glued without any mechanical constraints and have a straightness requirement on the sagitta of less than 300 μm .

One of the main innovations of the RD6 prototype, namely the use of carbon fibre reinforced Kapton® straws, was retained in the present TRT end-cap design. As described in section 3.2.2

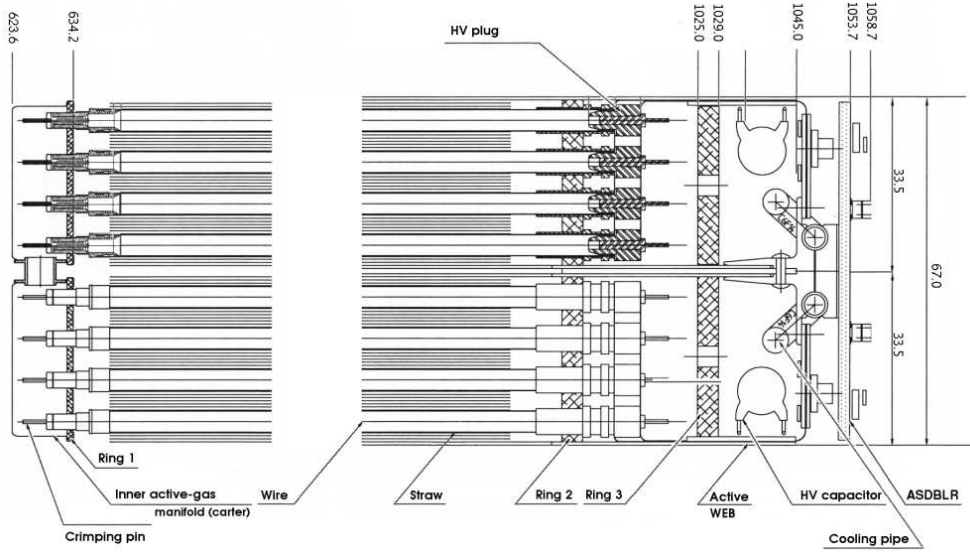


Figure 2. Basic layout of eight plane wheel which consist of two back-to-back four plane wheels with the straw and wire connection at the inner and outer radius. In this figure the inner radius is to the left and the outer is to the right. The layout is shown for type-A wheels and all distances are in mm.

each straw is reinforced with four carbon-fibre filaments running along its length. This reinforcement reduces the straw deformation due to temperature and humidity variations and improve electrical properties of the straw. However, the outer surface of the reinforced straw is no longer cylindrical and would lead to a challenge in the accurate positioning of the straw and gas tightness of the wheel. In addition the straw wall is kept at high voltage. For both of these reason the straws are equipped with insulated end plugs prior to their insertion into the wheel.

The straws are capable of supporting their own wire tension of 60 g without buckling or significant deformation. This is an important design feature, since it simplifies the assembly and decreases the risk of observing bent straws in the finally assembled detector. The combination of carbon-fibre reinforced straws and lightweight carbon-fibre rings, gives a mechanical structure with low mass: the support structure for the straws and radiators (ring 1 and ring 2) weighs 0.9 g per straw. This has to be compared to a weight of 0.7 g for a reinforced straw (without end plugs), to which the carbon-fibre strands contribute $\sim 30\%$.

A complex rigid-flex printed-circuit board, referred as the WEB (Wheel End-Cap Board) provides high voltage and signal connections for the end-cap wheels through two separate flexible layers (figure 3). Each flexible layer, made of polyimide, has conductive paths from a signal or HV connection on the rigid part of the board to holes with six inward-pointing petals that are forced by a plastic plug against the inner wall of the cathode to make the electrical connection to the straw. The WEB petals are shown in figure 4.

The signal (anode) connection is done in an analogous way using a second flexible layer, also containing holes with metallic petals. A press-fit between petals in the signal layer and a metallic crimping pin inserted into the outer end plug positions and electrically connects the anode wires. A copper crimping pin covered by plastic is inserted into inner end plug and fixes the anode wire at the inner radius.

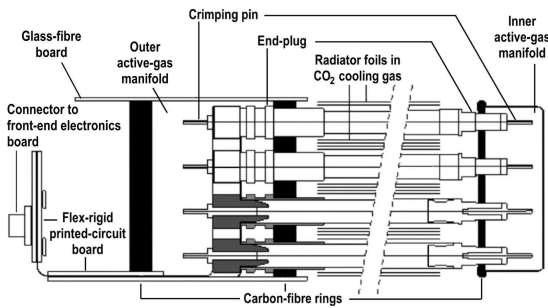


Figure 3. Schematic view of the TRT end-cap wheels, showing the plastic end plugs used to position and fix the straws in the inner (right side of this figure) and outer (left side of figure) C-fibre rings, the crimping pins holding and positioning the wires, the inner and outer active-gas manifolds, and the flex-rigid printed-circuit board on the left used to connect the straws to high voltage and the wires to the front-end electronics.



Figure 4. The flexible layers of a Wheel End-Cap Board (WEB) with the conductive paths for a signal from anode wires to the rigid part of the board. The anode wires are connected to the path via a crimping pins (one seen on the photo) through holes with six inward-pointing petals.

A third C-fibre ring at the outer radius is glued to the rigid part of the flex-rigid printed circuit board and to a simpler glass-fibre board, referred as passive WEB, on the opposite side of the four-plane wheel. This design provides a rigid structure around the outer wheel perimeter that also serves as the outer gas manifold. The inner gas manifold is made from reinforced polyimide material.

Two four-plane wheels are held together as a eight plane wheel through a set of temporary short axial metallic tie-rods at the outer radius and by gluing of input and output connectors of the gas manifolds for the both wheels on the inner radius. The temporary short metallic tie-rods are replaced by permanent long tie-rods during the stacking of the wheels into the final mechanical unit.

The whole eight plane wheel is covered with a thin metal-clad polyimide membrane on each $r\phi$ side and at the inner radius. The metal cladding of the membrane provides a signal-return path from the inner radius of the straw to the outer radius, where the electronics ground is defined. Additional membranes are used to provide a CO₂ cooling gas envelope. The cooling gas is required to remove the heat that is generated in the straws as the positive ions, created by the ionizing particles, drift to the cathode.

The ionization current heat dissipated in the straws is removed through the CO₂ cooling gas, which enters each eight plane wheel at its inner radius and then flows out along the straws and radiators foils. The cooling gas itself is cooled in a metallic heat exchanger located at the outer radius between groups of one or two eight plane wheels, and then flows down to the next wheel. The heat dissipation depends directly on the straw counting rate and is estimated to be 10 to 20 mW per straw at the design LHC luminosity. In order to maintain straw operational stability and gas-gain uniformity, the temperature gradient along a straw should not exceed 10°C. In addition, the flow of CO₂ evacuates any xenon gas which might leak out of the straws. Xenon in the inter-straw region could absorb transition radiation photons and degrade the electron identification efficiency of the TRT.

The assembly of the end-cap modules was performed at two assembly sites in Russia: PNPI [10] and JINR [11].

3. Description of the eight plane wheel components

All components used for TRT end-cap assembly are expected to remain stable over a period of 10 years at ambient temperature (with temperature gradients not larger than 20°C across TRT end-cap detectors) under the radiation environment expected at the LHC (not more than 10 Mrad integrated dose over 10 years of operation) and exposed to a gas environment composed of CO₂, O₂ and Xe.

3.1 The carbon fiber rings

The TRT end-cap support rings are the key elements of the mechanical structure of the TRT end-cap wheel. In order to achieve the required overall accuracy together with light weight, the support rings are manufactured in composite materials with specific tolerances of some tens of microns. The choice of material is based upon five criteria: the transparency to particles, the mechanical behaviour, the radiation hardness, the low out gassing and the low gas permeability. On the basis of the above requirements, high performance Carbon Fibre Reinforced Plastic (CFRP) was selected to be used to manufacture the rings. The ring matrix is epoxy resin and the material has the following general properties:

- radiation hardness of resin² ≥ 10 MRad [12];
- circumferential coefficient of thermal expansion (CTE) $\leq 4 \cdot 10^{-6}$;
- curing temperature of resin $\leq 120^\circ\text{C}$;
- polymerisation degree of resin $\geq 95\%$;
- the lay-up of fibres is balanced and symmetric for all rings and, in addition, “quasi-isotropic” for rings A1 and B1 (see table 2).

The radial dimensions, thickness and height of the six different ring types made in CFRP can be found together with other properties in table 2. Each of these rings is perforated by a large number of precise holes (~ 3000). The positioning accuracy of the holes is crucial to the physics performance of the detector. The required tolerances for these holes are: circumferential positioning $\leq \pm 10''$ and axial positioning $\leq \pm 0.02$ mm.

The TRT end-cap rings support the TRT straws. The first ring (A1, B1) or inner support ring at the innermost radius is used to position and fix the straws and is a part of the inner enclosure. The straws are inserted and glued into precisely drilled holes in an inner (A1, B1) and outer (A2, B2) ring. Good mechanical stability of the assembly is ensured at the outermost radius through the beam-like structure formed by the two outer support rings (A2, A3) and (B2, B3) and their flanges (the active and passive WEBs glued to the support rings).

The CFRP rings are electrically conductive and should be at ground potential. Because the rings have a direct capacitance coupling to the signal connectors, it is necessary to make a low

²Almost all epoxy resins are quite radiation-hard and can easily tolerate a dose of more than 50 MRad

Table 2. Properties of the six TRT end-cap ring types made in Carbon Fibre Reinforced Plastics (CFRP).

Type of ring	Outer diameter of ring (mm)	Ring thickness (mm)	Height of ring (mm)	Ring flatness (mm)	Number of holes	Diameter of holes (mm)	Holes function
A1	1268,4 _{-0,5}	1,2±0,1	31,4 _{-0,2}	≤0,1	96	2,1 ₋₀ ^{+0,06}	grounding pins straw
					3072	3,0 ₋₀ ^{+0,03}	
A2	2006 _{-0,5}	4,0±0,2	31,4 _{-0,2}	≤0,1	192	2,1 ₋₀ ^{+0,06}	grounding pins straw
					3072	5,3 ₋₀ ^{+0,03}	
					192	2,1 ₋₀ ^{+0,06}	grounding pins reference for assembly
					4	3,0 ₋₀ ^{+0,075}	reference for assembly
A3	2058 _{-0,5}	4,0±0,2	30,4 _{-0,2}	≤0,1	14	4,0 ₋₀ ^{+0,075}	gas connectors
					2	4,0 ₋₀ ^{+0,075}	
B1	1268,4 _{-0,5}	1,2±0,1	54,9 _{-0,2}	≤0,1	96	2,1 ₋₀ ^{+0,06}	grounding pins straw
					3072	3,0 ₋₀ ^{+0,03}	
B2	2006 _{-0,5}	4,0±0,2	54,9 _{-0,2}	≤0,1	192	2,1 ₋₀ ^{+0,06}	grounding pins straw
					3072	5,0 ₋₀ ^{+0,03}	
B3	2058 _{-0,5}	4,0±0,2	53,9 _{-0,2}	≤0,1	192	2,1 ₋₀ ^{+0,06}	grounding pins reference for assembly
					4	3,0 ₋₀ ^{+0,075}	reference for assembly
					14	4,0 ₋₀ ^{+0,075}	gas connectors
					2	4,0 ₋₀ ^{+0,075}	

**Figure 5.** The TRT end-cap rings A1 and A2.

impedance electrical connection between the ring and the detector signal return ground. This connection is made by gluing special contact pins into holes drilled in the rings.

The rings were industrially produced at the Perm “Mashinostroitel” company (Russia) [13]. The quality control procedures used are designed to verify conformity to the technical specifications. The contractor has measured all the relevant properties of the ring and guaranteed its conformity before packing for delivery to assembly sites in Russia. The following measurements of each ring were made:

- ring dimensions measurements - the height and the circumferential positioning of the holes, the real diameter of the holes, the diameter, height and wall thickness of the rings, ring not-flatness;
- ring deflection under load to check the overall mechanical behaviour of each manufactured ring;
- amount of the fibers and resin in the ring material;
- Young’s module measurements under traction and bending for each ring;
- polycondensation value of resin by a extraction method;
- circumferential coefficient of thermal expansion;
- visual inspection.

The TRT end-cap support rings delivered to assembly sites passed through Input Quality Control (IQC) procedures at each site. These procedures include the following measurements: ring not-flatness, height of the ring, the ring thickness, hole diameter, ring’s deflection and visual inspection. The results of the IQC at the assembly sites and the control procedure at the company were used to create a passport for the each ring. The passport was uploaded to the production data base and are accessible through a Web interface.

3.2 The detecting elements: straws-preparation and quality control

The straws are straight thin-walled circular tubes, approximately $70\text{ }\mu\text{m}$ thick, with an internal diameter of 4 mm. The straws as produced are 1660 mm long. The design, production and performance of the straw are described in detail in other documents [14, 15].

A straw is industrially produced [16] by helicoidal winding and bonding together two thin strips of polyimide film coated with aluminum and graphite on one side and polyurethane on the other. The polyimide film is a Kapton[®] 100VN film, $25 \pm 2.5\text{ }\mu\text{m}$ thick. The main challenge was to obtain a satisfactory final product complying with the stringent mechanical specifications (e.g. the diameter tolerance). A total of about 200,000 straws were manufactured.

3.2.1 Straw reinforcement

The straws as wound are affected by environmental factors, such as humidity and temperature, and can significantly change size or even lose straightness. In order to ensure mechanical stability and rigidity for each individual straw, four carbon fibre strands are impregnated with epoxy resin and bonded along the full length of each straw at 90° with respect to each other.



Figure 6. View of Straw Reinforcement Machine at the PNPI assembly site.

The implementation of such a reinforcement procedure for the production of all $\sim 200,000$ straws has required the design and fabrication of an automated straw reinforcement machine. The operating principle of this machine relies on:

- putting four C-fibre strands of equal length under the same tension;
- impregnating them with a known amount of epoxy resin;
- depositing them longitudinally along the outer straw wall;
- providing simultaneous polymerization at both ends of the straw.

The Straw Reinforcement Machines (SRM) were designed and constructed at CERN by the technical support (TA1) group. Two SRMs were set up at the assembly sites, one at PNPI and another at JINR. Figure 6 shows the machine at PNPI. A total of $\sim 106,000$ straws were reinforced at PNPI and $\sim 90,000$ at JINR from 1999 to 2002.

The straw curvature or straightness is an important parameter which was measured for each straw after reinforcement. The straws were categorized into four batches according to their deviation from straightness (see table 3). The straws that were more than 8 mm from straight were rejected. A special machine was designed to measure straw straightness. A straw inserted into a centered tool at the top of the machine is rotated around its vertical axis at 30 rpm. The curvature is measured by six photoelectric sensors spaced one mm apart as a maximum deflection from the vertical axis at the bottom of the 1660 mm long straw. One straw could be measured in about 15 seconds. The straws were sorted into bins corresponding to the location of the photo-sensors. After reinforcement, the outer diameter of every straw was measured using a gauge of 25 g with a hole of

Table 3. Distribution of categories of the straw straightness for all reinforced straws from beginning to end of production.

Straws category	Number of straws	%
< 3 mm	77,974	40.73
3-4 mm	46,945	24.52
4-8 mm	62,907	32.86
> 8 mm	3,599	1.88
Total	191,425	

$4.39^{+0.01}_{-0}$ mm diameter. The gauge was required to fall freely under its own weight along the full length of the reinforced straw from the top to bottom with the straw vertical. The diameter of the straw after reinforcement is an especially important parameter for the TRT barrel production as the straw, when inserted into a Barrel, must pass through holes of very tight tolerance ($+0.03/-0$) in the radiator sheets, dividers, and HV plates [6]. The resulting numbers of reinforced straws which passed all the tests are listed in table 3. The production yield was approximately $\sim 98\%$.

3.2.2 Straw production and quality control

The 1660 mm long reinforced straws destined for production use in the end-cap were cut into four straws of ~ 400 mm length. This procedure was called “precutting” as the length is not yet precise and was chosen only for convenience. Precut straws pass through a test of inner surface conductivity as high voltage distribution and signal propagation along straw depend on its resistance. At that time conductive epoxy is placed around one edge of the straw to provide conductivity between inner and outer surfaces.

After that the plastic end plugs which provide isolation of the straw from support rings, gas distribution into straw, wire fixation and fixation of straw in the support rings were glued to the straw. The final step to get the precise length of the completed straw of 372 ± 0.1 mm was to cut the outer end plug.

The now fully equipped straw was sent through several quality tests. First it was checked for gas-tightness. Sets of 8 straws were installed into special tooling (figure 7) producing two different gas volumes: one inside the straws, another outside. An overpressure of 1 bar was created inside the straws volume and after 30 seconds of temperature stabilization an increase in the outer volume pressure was observed in case of a straw leak. If the pressure drop inside the straws was more than 0.1 mbar/bar/min, each individual straw was retested to identify the leaking one. This technique was fully automated except for the insertion of the straws into the tooling.

Then the straw was simultaneously checked for straightness and length (figure 8). A CCD camera was moved along a straw that was rotated on its axis. A number of photos were made at different straw rotation angles and at successive points along the straw and analysis of this information gave the straw straightness value. Measurements of straw length were performed through determination of the position of the straw ends with CCD camera comparing each straw with a standard straw. The criteria for an accepted straw were to have a saggita less than $200 \mu\text{m}$ and a length accuracy better than $100 \mu\text{m}$. The last step was a visual inspection. During this procedure the operator checked each straw for any damage, bubbles in glued parts, runs of glue etc..

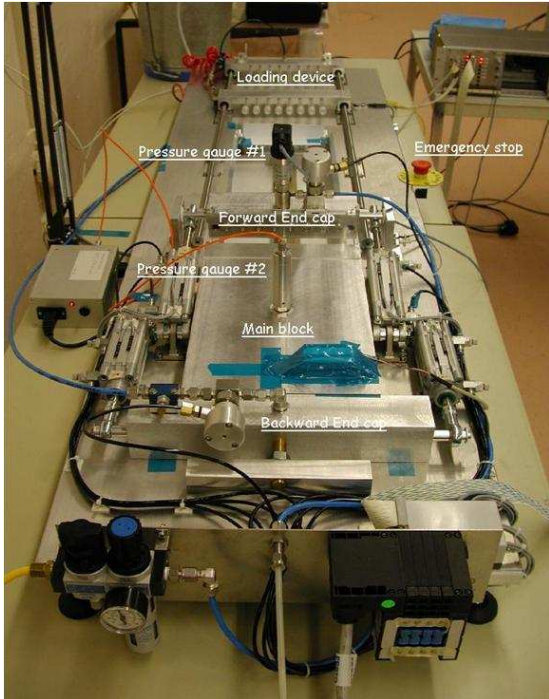


Figure 7. The machine checking straw tightness. The reached sensitivity was about 0.1 mbar/min/bar. Eight straws were measured simultaneously.



Figure 8. The machine measuring straw straightness and length.

Straws category	Number of straws	%
< 100 μm	178,809	63.15
100 – 200 μm	92,939	32.82
200 – 300 μm	11,418	4.03
Total	283,166	

Table 4. Distribution of categories of short straw straightness for all accepted straws produced at both assembly sites.

Two special workshops were organized at the assembly sites in PNPI and JINR to provide production and testing for short straws. These workshops produced and tested more than 170,000 short straws for A-type wheels and more than 112,000 short straws for the assembly of B-type wheels.³ The production yield was approximately $\sim 91\%$.

Table 4 summarizes the distribution of categories of straw straightness for all accepted straws produced at both assembly sites over the period 2000 to 2004.

³More than 79,000 straws were also produced for C-type wheels. Originally the TRT end-cap was designed with an extension up to $|\eta| < 2.5$ ($|z| < 3363$ mm) using a third type of wheel, C-type. The C-type wheels were designed to contain 4608 straws positioned in eight successive layers spaced by 8 mm along z (as for A-type wheels). Each layer, however, contained only 576 straws in the azimuth plane, a lower density and smaller number than for the A and B-type wheels. The straws C-type were also planned to be longer by 14 cm than straws A and B-type to extend η -coverage of the TRT end-cap. The construction of C-type wheels was been staged and have not been assembled.

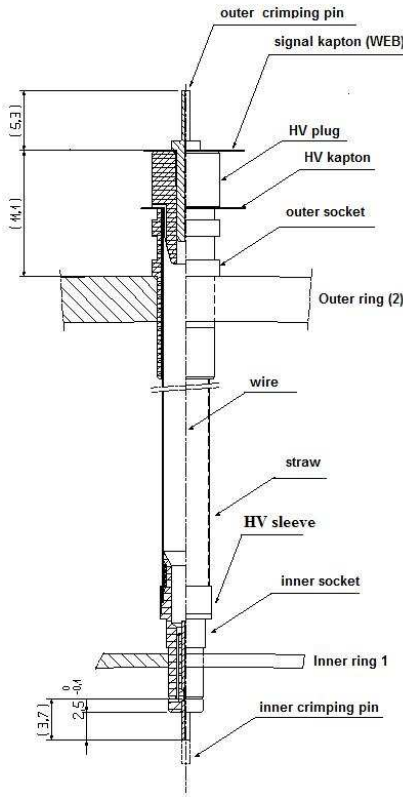


Figure 9. Detail of a straw as assembled in the detector.

3.3 Connecting and insulating straws: high voltage plugs, insulation end plugs and crimp pins

Figure 9 shows a schematic view of the assembly of one straw with the wheel support rings (ring 1 and ring 2). The straw's connecting elements, three types of end pieces made of precision plastics parts, namely the inner insulation socket, the outer insulation socket and high voltage connector, and the internal anode wire, fastened by crimp tubes on both sides are also visible. In order to achieve the required overall measurement accuracy of the detector the connecting plastic elements had to be manufactured with an accuracy of some tens of microns. A total of about 2,000,000 connecting elements of five different types were fabricated from the beginning of 2000 to the middle of 2003. Figure 10 is a photo of the various types.

3.3.1 High voltage plugs

The high voltage plugs are custom machined parts that provide a reliable connection from the high voltage to the straw cathode. The high voltage plugs are inserted through the flexible layer of the WEB into the straw, so that the petals of the flexible layer are forced into contact with inner straws walls. The high voltage plugs were manufactured in pure polyetherimide (PEI) [17]. Along the surface of the high voltage plug is a groove with a width and depth of ~ 0.3 mm which serves as a way to feed the active gas mixture into the straw.



Figure 10. From left to right: high voltage plug, outer and inner end plug, outer and inner crimp pin, and high voltage sleeve.

3.3.2 Insulation end plugs

Two different sets of precision plastics parts, the outer insulation end plugs and the inner insulation end plugs, were used to connect the ends of the straws to the structure (CFRP rings) of the TRT end-cap wheels. The functions of the end plugs are the following:

- to accurately position and hold the ends of the straws in the support ring (CFRP);
- to precisely locate, to better than 50 microns, the anode wires with respect to the axis of the straws;
- to ensure absolute stability in time;
- to ensure gas tightness;
- to electrically insulate the straws, which are at high voltage (typically 1530 V), from the wires and the grounded and conductive CFRP rings.

The functionality of the end plugs, during the assembly of the TRT end-caps, relies on a high level of surface finish and on tight dimensional tolerances for the plastic parts. The baseline material selected for the end plugs is Ultem[®] (General Electric Plastics) [18], an unreinforced amorphous thermoplastic polyetherimide (PEI), of grades 1000 or 1010. The choice of raw material was based upon the following criteria:

- low viscosity for hard-to-fill parts;
- low interaction cross-section for ionizing particles;
- mechanical behavior: stiffness, stability, etc.;

- radiation hardness;
- low out gassing, low gas permeability;
- good adhesive bonding properties;
- good transparency (to allow visual inspection of the glue joints);
- high dielectric strength.

All the end plugs were manufactured using injection-molding. For each production batch, 1% of each end plug type was used to carry out verification tests which included a visual as well as geometrical dimension and tolerances check. The delivery was spread from the beginning of 2000 to the middle of 2003.

3.3.3 Crimp pins

The anode wire, a $\sim 30\text{ }\mu\text{m}$ gold plated tungsten wire is the critical element for the detection of particles. The position and tensioning of the anode wire is ensured by mechanical crimping of small precision ($10\text{-}20\text{ }\mu\text{m}$) metal tubes mounted in the two end plugs.

The crimp pins used to fix the anode wire at the ends of the straw were custom designed for the end-cap. The precision metal parts (oxygen free copper - ISO Cu-DHP 99.90) used on the inner radius of the end-cap straws were over-molded with a plastic insulator as shown in figure 10. This inner crimp pin has a purely mechanical function. The outer crimp pin, in addition to the role of positioning the wire, also connects the fast electrical signal to the readout board and is, therefore, electro-plated with gold. In both cases the $30\text{ }\mu\text{m}$ anode wire had to thread easily through the pin during assembly.

The crimping pins has a length between 12.5 and 13.3 mm, an outer diameter between 0.7 and 2.5 mm and internal hole diameter of 0.1 mm. For the critical characteristics, such as the outer diameter, inner diameter and concentricity of hollow parts, frequency histograms of the measured values were provided by the supplier.

The delivery of 700,000 crimping pins of two types used to hold the anode wires, was spread over the period 2000–2002.

3.3.4 High voltage sleeves

The straw walls serve as the TRT cathodes and are operated at a voltage of $\sim 1530\text{ V}$. At the same time the minimum distance between two adjacent straws on the inner radius is about $\sim 1.2\text{ mm}$ and $\sim 2\text{ mm}$ between straws and the carbon fiber inner ring which is at ground potential. To decrease probability of any discharge between two adjacent straws at non equal potentials and between straws and inner ring an additional thin cylindrical ring or HV sleeve was mounted onto the outer straw surface at the inner end (figure 9). The HV sleeves was made from Kapton[®] by helicoidal winding and bonding together two thin strips of polyimide film cut to a length of 3.3–3.5 mm. The wall thickness of the HV sleeve is $\sim 0.075\text{-}1\text{ mm}$. Internal diameter is $\sim 4.400\text{-}4.415\text{ mm}$, i.e. slightly more than the straw outer diameter.

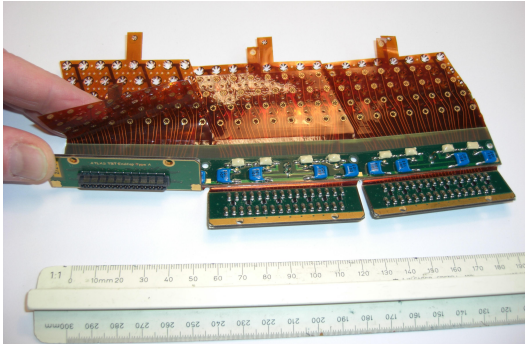


Figure 11. A Wheel End-Cap Board (WEB) for type A wheels. The main parts of the board, the baseplate containing HV protection capacitors (blue elements), HV connectors and fuses (grey elements), the three flaps each containing protection resistors and a connector and finally the two Kapton® flex parts for signal and HV connection can be seen.

3.4 The Wheel End-Cap Board (WEB)

The active Wheel End-Cap Board (WEB) is the interface between the straws on one side and the readout electronics and high voltage on the other side. The active WEB, an important part of the mechanical and structural framework of the end-cap wheels, is a printed circuit board consisting of two flex Kapton® multi-layers sandwiched between two rigid printed FR-4 [19] boards (figure 11). A special and innovative design was introduced to minimise the mass of material used in the detector as well as to simplify the assembly procedures for the 250,000 straw channels.

A single board connects 96 straws to their readout channels and supplies three groups of 32 straws with the necessary high voltage (see figure 12).

The size of an individual board is approximately $95 \times 210 \text{ mm}^2$ and its main parts are a baseplate containing HV protection capacitors, HV connectors and fuses, three flaps each containing protection resistors and a connector and finally the two Kapton® flex parts for signal and HV connection. The lengths of the flex parts are different for A and B type wheels.

The active WEB consists of the following main components (figure 13):

- a single sided printed circuit board with a thickness of 0.6 mm and $35 \mu\text{m}$ of copper covered by thin layer of Ni-Au (baseplate);
- a double sided $50 \mu\text{m}$ Kapton® layer with two layers of return signals;
- a single sided Kapton® layer for high voltage distribution;
- a single sided printed circuit board with a thickness of 0.6 mm that serves as shielding.

The baseplate part of the WEB is designed as one of 32 segments in ϕ of a circle that forms a seal for the active gas volume between the outermost rings 2 and 3. The high accuracy needed to glue the plates together to make the seal is achieved using three baseplate reference holes which

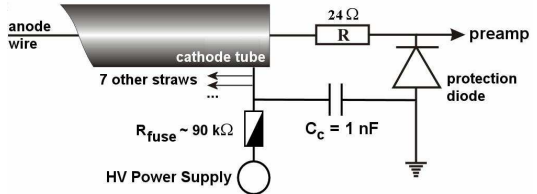


Figure 12. Straw high voltage and signal connection scheme. Straws are connected in groups of eight to the HV.

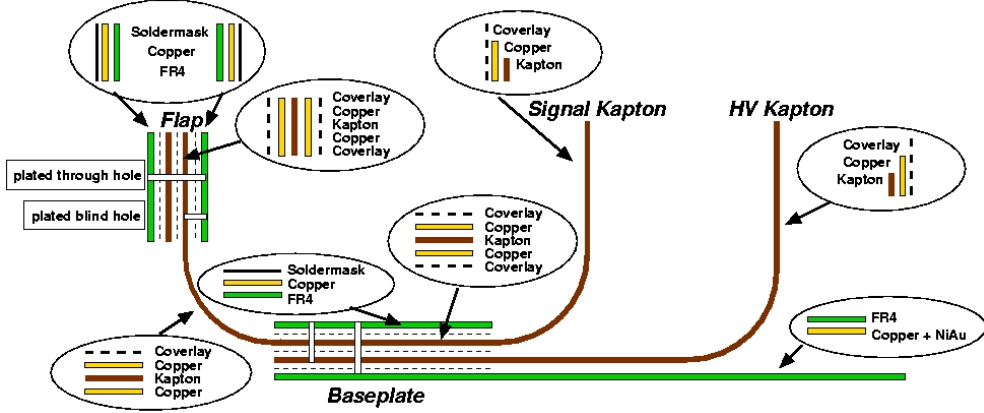


Figure 13. An overview on WEB multi-layer structure. In between the layers of the baseplate and the flaps, layers of glues are indicated by dashed lines.

were positioned in the assembly jig. On one side, the baseplate is equipped with twelve capacitors of 1 nF to couple the signal return from twelve HV channels of eight straws each to the electronics reference ground. In addition to the capacitors, for each of these groups there is a fuse that can be used to disconnect a HV group in case of some irreparable HV problem (e.g. broken signal wire). The high voltage connection to each group of 96 straws is supplied via three sets of pins and the voltage is distributed to the high voltage flexible Kapton® circuit through 24 blind vias with a diameter of 1.2 mm. The other side of the baseplate is fully covered by a copper layer which is part of the signal-return path and Faraday shield of the detector. Twelve plated-through holes with a diameter of 300 μm connect the ground of the two sides of the plate.

In addition to the custom fuses developed for the TRT, a special device [20] was developed to allow remote manual burning of a fuse using pulses with a voltage of about 1500 V, a frequency 2 kHz and a current of up to 16 mA. Two types of high voltage problems that might call for a fuse to be burned are straws with broken anode wires and straws with a large displacement of the anode wire due to deformation of the straw wall or other parts of the mechanics.

A broken or displaced anode wire can, via repeated discharges, burn a hole in the straw wall which might cause a gas leak. In addition, either type of repeated discharge represents a large source of RF noise that disturbs the sensitive front end electronics throughout the Inner Detector. On the other hand, the fuses should be stable against infrequent single discharges not connected with large displacements. These custom fuses are the result of an extensive research study which took into account temperature, environmental and vibrational effects, stability against radiation damage and the necessary requirement of maintaining a very large fuse resistance after opening. The fuse uses a titanium strip on a lithium niobate plate (LiNbO_3). The burning time for the TRT end-cap fuse is 15-40 ms in the case of an anode-cathode short and 60-200 ms in the case of an anode wire tension loss. In normal conditions it is expected that the HV power supplies would trip early in such a discharge cycle and the manual fuse burning device would be used, after detailed analysis, to open the fuse in the problem area. The leakage current of a burned fuse is less than 10 nA.

On the WEBS axial leaded ceramic capacitors of 1 nF were mounted to serve as filters for the

high voltage. The capacitors are rated for 2.5 kV. Long term (2-3 weeks) static tests at 3.125 kV were performed with all capacitors. Capacitors which developed a short or were showing any sign of leak current were rejected. A subset of the capacitors were tested in a static test of six months. In total about 2% of the tested capacitors failed the tests and were rejected.

A dynamic test was performed on 1% of each batch of capacitors using a series of 500 Hz and voltage of 2.2 kV discharges. There were no failures from this test.

The flaps of the WEB are bent 90° perpendicular to the baseplate at final installation and carry the anode signals to the ASDBLR electronics board via a connector as shown in figure 2 such that the electronics board are like the tread on the surface of a tyre (see figure 14). The flaps are held in position by non-magnetic screws threaded into an extension of the metallic cooling plates. Near each connector on the flap are mounted 32 protection resistors (24Ω), one for each straw channel, and eight quad protection diodes, one package for a group of four straws (figure 12). In total, 96 plated blind vias with a diameter of $800\mu\text{m}$ are connected to the rigid part of the flaps to the signal Kapton®. The connector-side of the flaps is connected to the resistors and diodes by 187 plated-through holes with a diameter of $300\mu\text{m}$. The smallest trace width and smallest distance between traces on the flaps is about $200\mu\text{m}$. To ensure high voltage stability of the board and to avoid any discharge on the WEB surface, the board is covered by a $50\mu\text{m}$ thick solder-mask except at the locations of solder pads. In addition, after soldering the passive electronic protection elements to the WEB, all boards were cleaned and an additional cover-layer of a urethane conformal coating Fine-L-Kote™ was sprayed on the surface of the baseplate and the flaps.

The two flexible Kapton® layers were introduced to allow a fast but reliable connection from the anode wires to the electronic readout and from the wall of the straws to the high voltage source. Each flexible layer consists of a main Kapton® layer of $50\mu\text{m}$ thickness on which the conducting copper traces for the high voltage or the signal are etched. To protect these traces there is an additional coverlayer of $50\mu\text{m}$ Kapton®. The signal and high-voltage lines end in “Daisy”-petal shaped Kapton®-Copper parts of the flex which during the assembly process are squeezed by a polyetherimide plug to produce an electrical connection. The HV plug is inserted into the straw through the petals to make the high voltage connection. While for the signal connection the “Daisy” petals are pushed into the HV plug by a metal crimp tube which also fixes the signal wire as shown in figure 15. To produce the structure of the “Daisy” petals in the Kapton® film, a novel technique was developed at and patented by CERN for chemical etching of Kapton®. As the flex Kapton® connects the four z layers in a sector of a four plane wheel, the WEBs used for type-A wheels have a smaller flex part compared to type-B WEBs where the z spacing between layers is larger.

In order to ensure viability in an LHC detector, the WEBs and all the component materials were tested to be radiation hard up to 10 MRad and up to 10^{14} neutrons/cm².

The most challenging and demanding tolerances for the fabrication of the WEBs (especially the reference holes used for assembly) are summarised in table 5.

3.4.1 Quality assurance for the WEBs

In addition to the standard quality control steps at the production company, the reliability and quality of the bare, unstuffed, WEBs were subjected to quality control steps by the collaboration:

- test of the geometry and the mechanical tolerances using a jig;

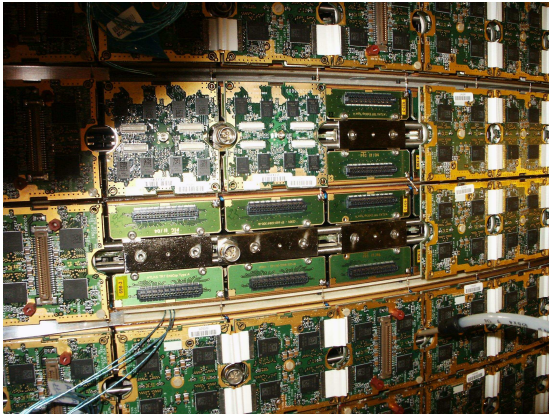


Figure 14. Readout electronics boards on stacked type A wheels. The bottom and top eight plane wheels are complete with time measuring DTMROC triplet boards with their distinctive white jumpers. The second and third wheel from the top show some analog ASDBLR boards as well as WEB flex connectors ready for ASDBLR boards.

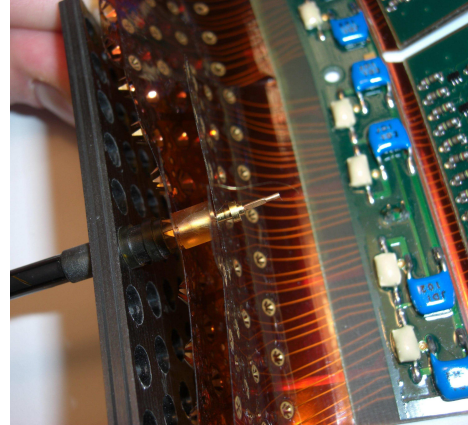


Figure 15. Connection of the high voltage and signal flex of the WEB to the straw end.

Table 5. Mechanical matching tolerances for the WEBS type-A and type-B.

<i>Element</i>	<i>Value</i>	<i>Tolerance</i>
Angular matching		$\pm 10''$
Diameter of reference holes	3.12 mm	$+12/0 \mu\text{m}$
Distance between reference holes		$\pm 20 \mu\text{m}$
Absolute position of reference holes		$\pm 50 \mu\text{m}$
Dimensions of the WEB	95×210 mm	$+100/0 \mu\text{m}$

- test of the mechanical stability of the multi-layers: the layers should not break or separate by applying a force less than 10 kg;
- visual inspection of the flexible layers (no cut, no broken trace, no damaged “Daisy” petals) and the rigid FR4 part (no broken traces, no cracks);
- for each batch (order of 100 boards), samples were tested to withstand a minimum of 80 bends of $\pm 90^\circ$ without any visible traces of material fatigue in order ensure robustness of the flexible Kapton® flaps;
- all vias and blind-holes were tested for conductivity and connectivity;
- HV lines (signal lines) had to stand 3000 V (2400 V) w.r.t. ground without measurable current ($< 1 \text{nA}$)

After the WEBS were equipped with the electronic components — connectors, resistors and diodes — the visual inspection and all conductivity and connectivity tests were repeated. The WEB production yield was about 60%.

Table 6. Spacer specification for TRT end-cap radiators given to the manufacturer.

<i>Spacer type</i>	<i>Density</i>	<i>Width</i>	<i>Desired film spacing</i>
A	$\sim 2 \text{ g/m}^2$	$\geq 2100 \text{ mm}$	$0.17 \text{ mm} - 0.21 \text{ mm}$
B	$\sim 4 \text{ g/m}^2$	$\geq 2100 \text{ mm}$	$0.30 \text{ mm} - 0.40 \text{ mm}$

After assembly of all wheels into the end-caps the fraction of non-working channels because of WEB defects was less than 0.5%. The remaining defects were largely caused by long term cracking in vias and blind-holes which interrupted and disconnected signal lines. This effect is most likely due to absorption of humidity or cleaning liquid by the Kapton® causing an expansion of the flexible layers resulting in large mechanical forces. During the end-cap assembly process, vias which showed these problems were repaired and strengthened by inserting a wire through the via and soldering it in place. The number of channels which needed a repair was on the order of one per thousand.

3.5 The radiators

The TRT end-cap radiators are disk-shaped stacks of alternating layers of thin plastic film and sheets of a spacer fabric, and are located in the gaps between adjacent straw planes. In the interest of minimizing material and complexity, no provision was made for stretching the foils to render them perfectly planar, nor to precisely control their spacing. Beam-test measurements had shown that the Transition Radiation (TR) performance of such non-regular foil radiators is close to that of ideal, regular foil radiators [21, 22].

Although entirely made from standard plastic materials, radiation damage is not generally considered a problem for the radiators. Some changes of the material properties under irradiation are assumed to be tolerable, since there should be little or no mechanical stresses in the radiators as mounted in the TRT end-cap wheels.

3.5.1 Selection of materials

Commercially available polypropylene film of $15 \mu\text{m}$ thickness was used for the radiator foils. It was delivered on rolls of 2200 mm width, and was perforated with one 2 mm^2 hole per 100 cm^2 of film, in order to allow the finished radiators to breathe easily in response to pressure or composition changes of the environmental gas.

A custom-produced synthetic net (tulle fabric) was used as spacer between successive film layers. The tulle is made from multi-fibre threads composed of 22 dtex⁴ polyamid fibres. Initial tests had been made with a commercially available tulle fabric used in MLIs.⁵ It had a mesh size of $1.4 \text{ mm} \times 1.7 \text{ mm}$, and gave a film spacing of about $180 \mu\text{m}$, but its density of 5 g/m^2 ($\sim 30\%$ of the film density) was 2 to 3 times larger than desired for the TRT end-cap radiators.

On our request (see table 6), the manufacturer agreed to evaluate the feasibility of two different tulle fabrics with lower density and higher transparency by increasing the mesh size. The second

⁴dtex, or decitex, is a unit of linear mass density used in textile industry, with $1 \text{ dtex} = 10^{-4} \text{ g/m}$.

⁵Multi-Layer Insulation — alternating layers of coated plastic film and spacer fabric (like in TRT end-cap radiators) used for thermal insulation in space and cryogenics applications.

Table 7. Properties of the series-production spacers used in the TRT end-cap radiators.

<i>Spacer type</i>	<i>mesh size</i>	<i>Density</i>	<i>Width</i>	<i>Average film spacing</i>
A	6 mm × 7 mm	~2 g/m ²	≤ 2050 mm	0.23 mm–0.27 mm
B	6 mm × 7 mm	~4 g/m ²	≤ 2050 mm	0.23 mm–0.27 mm

**Figure 16.** Picture of the type-A spacer fabric used for the TRT end-cap radiators.**Figure 17.** A radiator of an early batch showing ridges (see text).

fabric should provide a larger film spacing for use in the B-wheel radiators, where the available gap between straw planes is wider than in the A-wheels. The test samples received were very promising and essentially met our specifications, except that the effective film spacing of the B-type, for which a two times thicker thread was used, remained somewhat below 300 μm. A standard thermofixation finishing process with an acrylic resin was applied to the bare fabric to provide dimensional stability. Figure 16 shows a picture of the A-type sample-spacer.

The series-production spacer fabrics were made according to unchanged specifications. Unfortunately, however, the quality of the material received was of lower quality and had different properties than the earlier samples. The degradation was due to inadequate packing and transport conditions, and the fact that much larger amounts of material were wound up on a single mandrel. The properties of the series-production spacer fabrics are summarized in table 7. The average film spacing obtained with the A-type spacer was about 25% higher than for the test samples, and thus about the same as that of the B-type spacer. Moreover, the width of the fabric was below specifications (likely due to some shrinkage), with the consequence that the spacer sheets had to be stretched during radiator assembly. The stretched spacers in turn contributed to the problems (described below) with the quality of the first batches of radiators.

3.5.2 Radiator types and dimensions

Every four-plane wheel is equipped with 5 radiators: one in each of the three gaps between the straw planes, and one on the outer side of the first and last straw plane, respectively. The inside radiators for the A-wheels are labeled A1, and the two identical side radiators A2. The inside radiators for B-wheels are labeled B1, while those on the outside, which have different thickness envelopes, are labeled B2a and B2b. After eight plane wheel assembly, the B2a radiators are found on the outside, while the two B2b radiators fill the straw gap between the two four plane wheels.

Table 8. Properties of the 5 TRT end-cap radiator types. Maximum thicknesses in parentheses apply only to small regions around the mounting holes. The outer and inner diameter of the all type radiators are equal to 1976.0 ± 1.0 and 1284.4 ± 1.0 respectively.

Radiator type	Average weight (gram)	Maximum thickness (mm)	Number of film layers	Spacer type
A1	392	3.4	13–17	A
A2	194	2.1 (1.5)	6–7	A
B1	1074	10.4	26–34	B
B2a	251	2.6 (2.0)	8–9	A
B2b	420	4.1 (3.5)	15–16	A

Similarly, in eight plane wheels of type A, two A2 radiators fill the straw gap between the two four plane wheels.

All the radiators have the same circular shape and circular, concentric cut-out. The radial dimensions and maximum thicknesses of the 5 different radiator types can be found together with other properties in table 8. A total of 96 equally spaced mounting holes are located 10 mm inwards from the outer perimeter. Their dimensions are 3 mm \times 7 mm in the radial and circumferential direction, respectively. They were produced by pushing a hot tool through a hole of corresponding size in a mask. The small amount of melting plastic material produced bonds between the layers of film and spacer fabric around the perimeter of the locating holes. Everywhere else the layers of film and spacer are loose, without any attachments between them.

3.5.3 Assembly and quality control of the radiators

Ideally, the TRT end-cap radiators should have a uniform thickness and fill the gaps between adjacent straw planes completely, yet without risking to bend any of the straws. The most crucial parameters of the radiators are therefore their uniformity and maximum thickness. However, it is far from obvious how to specify these parameters precisely, and how to control each individual radiator to see if it conforms to the specifications. As basically loose laminations of very soft plastic films and spacer fabrics, the radiators exhibit a certain *cushion effect*, which implies that the exact shape (i.e. thickness profile) may vary as a result of very minimal forces. A given radiator may exhibit some soft bumps exceeding the allowable thickness, which however disappear already under a very small pressure. The maximum thicknesses given in table 8 are derived from the nominal spacing between adjacent straw planes, after subtraction of the nominal straw envelope diameter (4.4 mm) and an additional 0.2 mm margin.

The radiators were assembled in industry. All radiators were initially produced with the maximum number of layers (see table 8). Before packing for delivery to CERN, the contractor established a thickness profile for every radiator. For this thickness mapping, the radiators were pinned in their locating holes on a flat table, and a laser telemeter mounted on a rotating arm was used to measure the thickness in 96 points on four different diameters. A soft Nomex® sheet of uniform thickness placed on top of the radiator applied a well-known pressure during the measurement. Its weight per unit area of 530 g/m^2 , which is lighter than a B1 radiator, corresponds to a pressure that also the straws can support without bending.

Details of the assembly and quality control specifications and associated procedures had evolved well into the series-production of the radiators. Unfortunately, the majority of the early radiators unpacked at the assembly sites in Russia turned out to be either unusable or usable only with special precautions and — often — only after removing a few layers of film and spacer fabric. The quality of the radiators was obviously degrading in the period between the Quality Control performed by the contractor and their unpacking at the assembly sites. As an example, a radiator of an early batch exhibiting some ridges is shown in figure 17. Such ridges can normally not be removed completely, if they were already present during transportation.

It had taken several iterations to implement sufficient improvements to all the relevant procedures — from production through QC, to packaging for storage and transport. In retrospect, the following three points were probably the most crucial:

- every manipulation of a radiator risks to introduce irreversible non-uniformities, whose importance are prone to get worse with time;
- both during storage and transport, the radiators must be attached to a flat, semi-rigid support plate with pins inserted in all the locating holes in order to accurately maintain their proper geometry (circularity and radial dimensions) at all times;
- tensions in the spacer fabric, applied during the lamination process because of the too narrow width (c.f. further above), have to be released before the mounting holes are made and the circular radiators are cut out of the bare stack.

In order to get a sufficiently high yield of radiators passing the Quality Control, it was also necessary to reduce the nominal number of layers for most of the radiator types. Originally, the nominal number was the maximum appearing in table 8, while eventually any radiator was considered acceptable for wheel assembly if its number of layers was within the corresponding range given in the table. The loss in TR performance (fraction of high-threshold hits) for A-wheels equipped with A1 radiators of 14 instead of 17 film layers was estimated to be about 10%.

3.6 Sealing the active gas volume: carters, cavaliers and passive WEBs

The end-cap “carters” (figure 18), made from Kapton® JP polyimide films, are used to complete the enclosure of the working gas volume at the inner radius of each four plane wheel. Cut sections of film were formed in specialized moulds at 280-330 degrees Celsius and then slowly cooled. The formed sheets were then cut to final size on a custom jig and then reinforced with strips of fiber-glass.

The “U” shaped end-cap “cavaliers” (figure 19) are made from PEEK⁶ serves to join together pairs of carters and to provide the active gas connection between pairs of four plane wheels.

The remaining part used to complete the gas seal is the passive WEB, a simple one-layer fiber-glass board without any electronic components. The passive WEB has the same dimensions as the rigid part of the active WEB and completes the gas seal on the outer radius.

⁶Polyetheretherketone with 30% glass fibers.

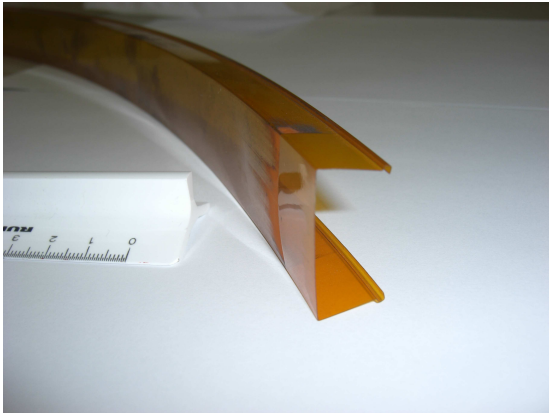


Figure 18. The end-cap “carter”, made from Kapton® JP polyimide film to enclose of the working gas volume at the inner radius of each four plane wheel. Eight carters were installed per each four plane wheel.

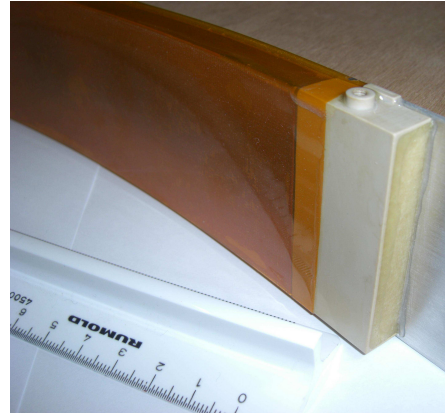


Figure 19. The end-cap “cavalier” serves to join together pairs of carters (one of them shown in the photo) and to provide the active gas connection between pairs of four plane wheels via the hole in the top part of the cavalier. Eight “cavalier” were installed per each four plane wheel.

3.7 Aging studies

As it was described in [15], at the nominal LHC luminosity the straw counting rate reaches the level of ~ 20 MHz and the average current can be as high as $0.15 \mu\text{A}$ per 1 cm of wire. After 10 years of operation this gives a total accumulated charge of about 10 C/cm . These conditions clearly require great care to avoid or minimize the various destructive ageing processes that can take place on the anode and cathode surfaces. In order to avoid such problems the TRT has consistently followed a strict validation policy for selection and control during assembly of the purity of all the components of the detector and the associated gas system. The basic criteria for component selection for detector construction are described in [12, 24]. About 1000 different types of tests were carried out in the process of detector and gas system production [25–27]. One of the primary lessons learned in these tests and worth repeating here is the need to absolutely avoid the use of components which contain or were ever in contact at any stage of production with organo-silicones. Unfortunately, this requirement is almost impossible to fulfill from ordinary suppliers, even those who claim processes free of organo-silicones. The tests described in the references above allowed the avoidance of many possible sources of serious contamination but, given the pervasive nature of these compounds, are not a complete guarantee.

4. Assembly of eight plane wheel

The assembly of an eight plane wheel was divided into several steps starting from the construction of a four plane wheel, the basic assembly unit. The four plane wheel assembly consists of two main parts, a “mechanical assembly” that puts together support rings, straws and WEBs, and then the wire stringing process. For either part quality control procedures were embedded wherever possible to ensure that the assembly was done correctly. Wheel assembly began at two assembly

sites in Russia in early 2001 and was completed in 2005. A total of 25 eight plane type-A wheels were assembled at PNPI and 17 type-B wheels at JINR.

Assembly took place on custom made very flat ($< 100 \mu\text{m}$) assembly tables made from aluminium alloy with precision holes (better than $50 \mu\text{m}$) to position the various items during assembly. The precision of the overall wheel assembly is defined by the precision of these holes, the flatness of the assembly tables, the precision of the tooling used to fix the wheel to the table and by environmental factors as a temperature and humidity. The most important assembly steps are discussed in sequence below.

4.1 The basic assembly unit: the four plane wheel

This section briefly describes the assembly of a four plane wheel which started from the procurement of components.

Each component, whether received from a manufacturer or produced in-house, was checked for conformance to specifications and cleaned before use. Some of the components went through several stages of sub-assembly before going into a wheel (straws, flex-rigid printed-circuit boards, inner gas manifolds). In these cases quality control was performed after each important stage of the assembly.

4.1.1 Assembly of the four plane wheels structure: rings, straws and radiators

The four plane wheel assembly process starts with the installation of the inner support ring (ring 1) and the inner of the two outer support rings (ring 2) on the precision assembly table described above. The rings are installed using nine accurately positioned tooling rods at the radius of each ring as shown in figure 20. The relative ring position in azimuth is defined by these rods so that after the installation the rings can be moved radially with respect to one another, but can not be moved either in azimuth or out of plane. Particular care has to be paid to the concentricity and relative angular position of these two support rings, since the accuracy of this positioning will determine the straightness of the straws after they are inserted into the rings.

The straws were inserted through the holes in the outer ring towards the inner ring. The straws were not supported along their length and therefore particular care has to be taken during their insertion into the holes in the C-fibers rings to preserve straightness and minimize the sagitta, which is required to be less than $300 \mu\text{m}$ after completion of gluing straws into the rings. Each straw was therefore inspected after insertion, both visually and using optical tools [28] and bent straws were replaced before gluing (figure 21). Following the installation and straightness inspection of the first plane of straws, the straws in that plane were carefully glued into position without any mechanical constraints (figure 22). The reinforced straws themselves become part of the wheel mechanical structure.

After the glue polymerization, which takes about 24 hours, the first radiator stack was installed above the glued straw plane. The radiator has a disk-shaped form with a total 96 equally spaced mounting holes located 10 mm inwards from the outer perimeter. These holes were used to install and stretch the radiator onto 96 temporary metallic rods fixed on the table. The installed radiator stack should be flat enough to fill the gap between the already glued straw plane and the straws which will be inserted on the next level above the radiator without risk of bending any straws.

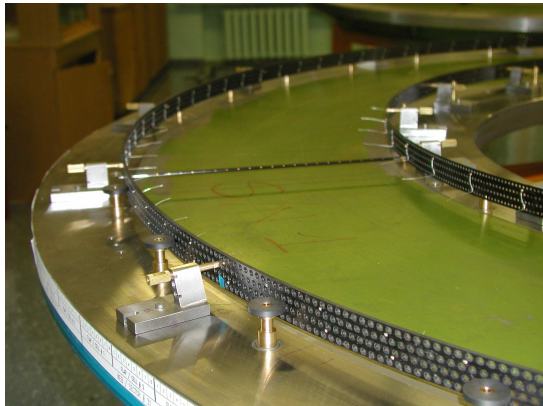


Figure 20. The inner and outer carbon-fibre rings installed on the assembly table. Tooling to support the rings and to make them round is also visible. One straw is shown inserted between two rings.

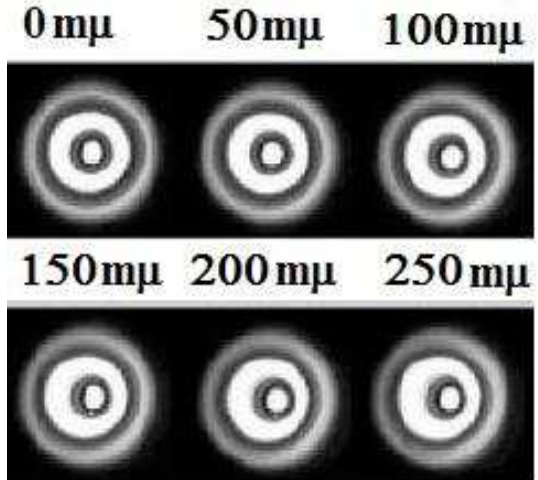


Figure 21. Straw straightness is inspected with the help of concentricity of the light pattern. The correlation of the light pattern with increasing bending of the straw tube is visible.



Figure 22. Gluing straws into the carbon-fibre rings.



Figure 23. Four-plane wheel undergoing a gas leak measurement. The cover closes the volume between the inner and outer rings. The twelve aluminium bars which clamp the table and cover are visible.

After gluing all four planes of straws between the outer and inner ring, and installation of three radiator stacks the assembled four plane structure can be removed from the assembly table using custom transfer tooling. The transfer tooling was designed to maintain flatness of partially assembled wheels and allow a high precision smooth lift from one assembly table to another.

4.1.2 Gas tightness test of the four plane wheel structure

The next stage was to re-check the straws for leaks. It was important to perform such test at this stage because the straws and their glued joints to the support rings are still easily accessible and repairable. A dedicated gas-tightness test checked the quality of the 3,072 glue joints between the

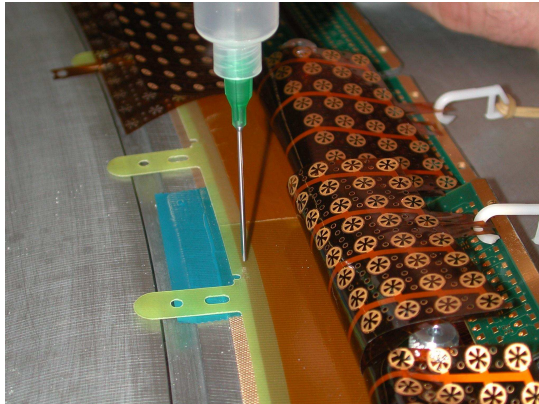


Figure 24. Active WEBs on the round assembly table being prepared for gluing onto the four plane wheel.



Figure 25. The four-plane wheel placed on the transfer tooling for lowering onto an assembly table on which active WEBs have been prepared for the gluing.

straws and their end plugs and between the end plugs and the support rings. The set-up used for the leak test consists of a flat steel table and a cover (both with thick wide rubber joints), a temperature sensor, pressure gauges and a clean system of valves and pipes connecting an argon bottle to the volume to be tested. The rubber joint is 20 mm wide and must be precisely positioned on the table and the cover must be centered with respect to the ring diameters. Gas tightness was achieved by uniformly compressing the rings onto the joints with the help of 12 aluminum bars that clamp the table and cover (figure 23). The gas tightness of the entire structure was estimated by measuring the leak rate of the closed gas volume filled with argon to 20 mbar over atmosphere. The leak rate (mbar/min/bar) was evaluated by measuring the pressure drop as a function of time.

A wheel was approved for subsequent assembly whenever the measured leak rate did not exceed 1 mbar/min/bar. Nevertheless, all effort was made to get a value as low as possible. A reasonable goal was to reach 0.1 mbar/min/bar.

4.1.3 Glueing of the Wheel End-Cap Boards

After checking the wheel gas-tightness the flex-rigid printed-circuit boards (WEBs) were glued to the outer ring holding the straws.

To glue the WEBs a special round aluminum assembly table was used which allowed vacuum clamping the WEBs to the table. The WEBs were installed one at a time on top of special protection masks on the table. Each WEB was installed and was located and held in position by fitting two dowel pins through corresponding holes in the assembly table.

Once all of the active WEBs were installed (figure 24), the wheel positioning tools were installed. To ensure that the WEBs remain flat against the table surface, a vacuum between WEBs and table was created.

Then the resin was applied to the WEBs and the wheel was lifted onto the active WEBs using the transfer tooling (figure 25) and the 12 alignment pins were inserted with a minimal force into the appropriate straws.

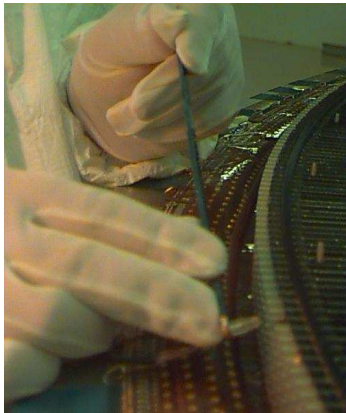


Figure 26. Insertion of high voltage plugs into the WEB.



Figure 27. The four-plane wheel during wiring. The wiring machine installed above the wheel.

After a curing period of 24 hours, the vacuum pump was switched off and the wheel was lifted using the transfer tooling. Once the detector was fully clear of the assembly table the quality of the glue joint was inspected. Special attention was paid to the gap between consecutive WEBS. If it was necessary to repair a faulty glue joint, the required amount of resin could be accurately added.

4.1.4 High voltage connection and insertion of wires

High voltage plug insertion is the next step after the gluing of the WEBS (figure 26). Before insertion, all straws were cleaned using ionized air. Each WEB high voltage flexible part was aligned with respect to its 32 straws so that outer ring of the high voltage petals coincided with straw diameter and then the flexible part was fixed using four high voltage plugs on four points corresponding to outermost straws. After that the remaining high voltage plugs were inserted.

To check quality of the electrical connections of the straws to their high voltage line a high voltage supply was connected to the flexible circuit and all possible leakage currents between high voltage and ground and between adjacent high voltage lines were verified to be below the specified threshold of 50 nA. Wherever necessary, poor connections were mended. After that the wheel was sent to the wire stringing.

Because a total of more than 250 thousand anode wires needed to be installed, a special wiring machine was designed for wire stringing (figure 27). The basic working principle of the wiring machine was to float the anode wire in a moving stream of air along the axis of a straw. The wire is fed from a spool into the center of the stream and into a feed tube which funnels the wire into the straw. The stream carries the wire through the straw keeping it centered and with minimal contact with the straw wall.

The wiring machine units were mounted on a secondary rolling table placed above the detector on the assembly table. A pneumatic crimping tool and a guiding jig for crimping tube installation was fixed on each side of the carriage for the two operators. On the outer side of the table near the guiding device there was a clamp for holding the wire end while a crimping tube was being installed in a straw. The crimping tubes for fixing the wire in the straw are crimped using the pneumatic tools. A wire tension block set for 65 grams of loading was located on a vertical rack on the inner side of the table. The tension block has two connected levers on an axis: the horizontal



Figure 28. The nose of the feed block fitted to blow the wire through the straw by the air stream (left). Insertion of the outer crimping pin into the hole of the HV plug (center). Wire crimping using the in-house fabricated pneumatic crimp tool (right).

lever with a load and the vertical lever with the wire clamp. This block, as well as the feed block, could be moved vertically and located opposite each straw layer.

There are a number of effects, including problems during crimping that can result in lower tension. Therefore the tension of the wires was measured during the stringing process itself and a final global wire-tension measurement for the whole four plane was completed before moving to the next assembly step. Before that final wire tension measurement the four plane wheel was exposed to gentle vibration to expose any latent slippage.

The acceptable values of wire tension during the wheel production were set to be between 55 and 75 grams. The upper limit was chosen to be comfortably away from the breaking tension ~ 220 grams, while the lower limit was high enough to allow good operation of the straw even with a few grams of slippage in the tensioning. The lower limit was defined from electrical instability of the wire which was found to be 35 grams, but, to be conservative, the operational criterion was increased to 55 grams. Less than 1% of the wires had to be restrung in routine operation.

Wire tension was measured using the standard method of putting a potential (~ 500 V) between the anode and cathode and then by vibrating or mechanically shocking the whole detector making the anode wire vibrate. The motion of a conductor in the electric field then produces a current which is maximized at the resonant frequency of the wire — a function of the wire tension. A simple current measurement vs. vibration frequency gave the tension for each wire.

For the end-cap wheels mechanical vibration rather than acoustic vibration was selected as an incomplete four plane wheel is difficult to excite with a loudspeaker and the resonance curves exhibited non-standard behavior such as multiple peaks.

The signals induced on the wires were amplified with a 16-channel custom made high input impedance amplifier and an input signal threshold of 1.5 mV. Signals were digitized by a PC based A/D board. The results of these measurements were recorded in the production database [29]. The corresponding frequency was translated into applied wire tension T in grams following the formula:

$$T = 4L^2F^2\mu/g, \quad (4.1)$$

where L is free wire length in cm, F is frequency in Hz, μ is mass per unit length in g/cm and g the gravitational acceleration. Uncertainties in the measured tension arise from variations in the wire diameter, the length of vibrating wire, and local deformations of straw tubes. The minimum uncertainty can be estimated as 1%. The results of these measurements were recorded in the production database.

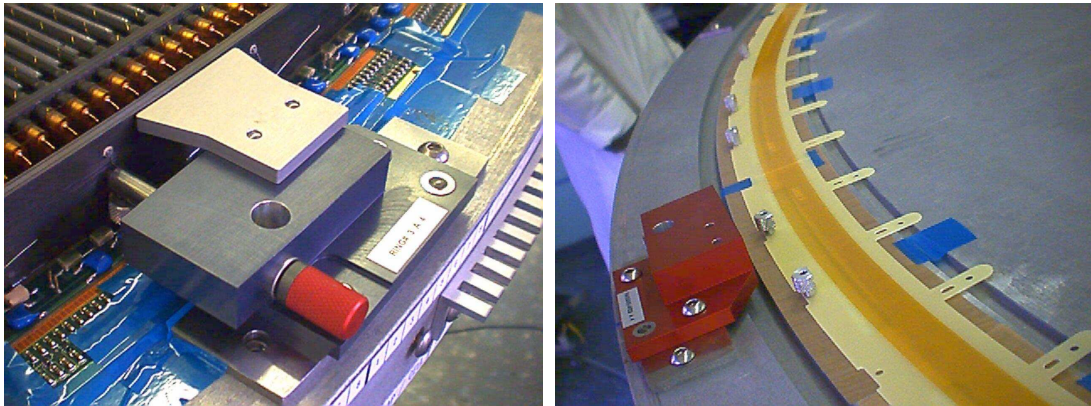


Figure 29. Third ring gluing. One out of 12 support tooling fixtures is visible.

Figure 30. Passive WEBs installed and fitted onto the assembly table for gluing to the four-plane wheel.

In the next stage, all electrical contacts between crimping pins and the connectors to the front-end electronics board were tested.

High voltage was then connected to the active WEB in its final configuration while the anode wires were connected to ground. The dark current was measured for all wires with a limit of 50 nA at 1800 V. If the dark current exceeded the specification limit then the problem wire was re-strung and the high voltage test and wire tension measurement was repeated.

4.1.5 Sealing of the active gas volume: assembly of third ring, passive WEBs and carters

After wiring the third and outermost C-fibre ring was prepared for gluing to the flex-rigid printed circuit boards (figure 29). After this gluing operation re-stringing becomes impossible and therefore all problematic wires and straws were investigated and repaired before the third ring gluing.

The method for gluing the third ring was similar to that used for gluing the active WEBs to the second ring. The four plane wheel was lowered onto an assembly table using the transfer tooling and the dowel pins were inserted into the WEB reference holes to position the wheel. A vacuum was used to clamp the whole four plane wheel to the assembly table. The epoxy resin was applied to the WEBs using the motorised dispensing fixture fitted to the assembly table.

Then the ring was placed onto the WEBs using the transfer tooling and 12 alignment pins were inserted into the corresponding holes on the ring. After a curing period of 24 hours, the vacuum pump was switched off and the wheel was ready for the next assembly step.

At the next stage the so called passive WEBs were glued to the second and third ring to close the gas volume at the outer radius. This procedure was similar to the procedure used for the gluing of the active WEBs and the third ring WEBs (figure 30). The passive WEBs were first aligned, positioned and fixed by dowel pins on the assembly table. Then the passive WEBs were vacuum clamped to the assembled table by the vacuum pump as were the active WEBs. A thin layer of resin was then applied to the appropriate surface of rings 2 and 3. Then the four plane wheel was lowered onto passive WEBs using the transfer tooling and after a curing period of 24 hours the wheel was ready for the next operation. As for the active WEBs, possible gaps between consecutive passive WEBs were filled by resin.

The final assembly steps were all related to the closure of the four plane wheel at its inner and outer radii. The gas volume at the outer radius may leak through the tooling holes in ring 3 which were used to align and fix this third ring during the gluing to the active and passive WEBs. Small PEEK parts were glued to these holes and two of them serve as the active gas connection to the four plane wheel. At the inner radius carters and cavaliers were glued to the first ring to close the gas volume (figure 31). The hole in the cavalier was used to provide gas connection between two four plane wheels after their assembly into an eight plane wheel. To complete the assembly of a four plane wheel the side radiators were installed into the wheel. Also the sector supports for the cooling plates and the active gas washers were installed onto one of the two four planes wheels which were assembled into an eight plane wheel.

4.2 Combining two four plane wheels to an eight plane wheel

The assembly of eight plane wheels was started with a dry assembly run of two back-to-back four plane wheels. Tooling holes had been placed in the part of the active and passive WEB protruding beyond the outer radius of ring 3. These holes served to position pairs of four-plane wheels and were also used to hold together the eight-plane wheel.

The lower production numbered wheel, the wheel with the sector supports and active gas washers, was fitted to the table, passive WEBs facing upwards and the wheel was secured to the table with a dowel pins. To reach a gas tightness volume between two four plane wheels, an O-ring was positioned in a groove between inner and outer insulated sector supports. The higher numbered wheel was placed on top of the lower numbered wheel on the assembly table. Both wheels were pinned in place by threaded rods. The alignment of all eight groups of cavaliers was checked to verify that the alignment was good enough to fit the active gas washers between cavaliers of two wheels without any modifications. The active gas washers were then glued to the cavaliers of the wheel fitted to the assembly table. The gas-tightness test of the volume between the two four plane wheels followed the dry run assembly.

The assembled eight plane wheel was lowered on the gas table. A special cover made with a honeycomb structure was used to close the volume. A flexible gas tight joint was installed on the gas table and the special cover at a radius of ~ 1027 mm, under the third ring.

The gas table and cover were then pressed slightly together by eight clamps which also secured the cover in position. The wheel gas inlets and outlets were used to fill the volume with argon gas and to measure the pressure drop inside the volume. The leak rate was required to be of the order of 1 mbar/min for 5 mbar over pressure. Once the CO₂ leak rate was at an acceptable level, the eight plane wheel was thereafter treated as a final unit, never again to be split into four plane sections.

To complete the assembly of the eight plane wheel, the cooling tube supports, HV cable and HV connectors were then fitted to the structure followed by closing and aligning the WEB flaps.

The whole r- φ surface of the eight plane wheel was covered with a thin metal-clad polyimide membrane on one side for wheel type-A and on both sides for wheel type-B. On the inner radius both gas seal carters were enclosed by metalized carters (seven per wheel).

The metalized carters and membranes provide a high frequency signal-return path from the inner radius of the straws to the outer radius, where the electronics ground was defined and as well as electrical shielding. Additional membranes were used to provide the required path for CO₂

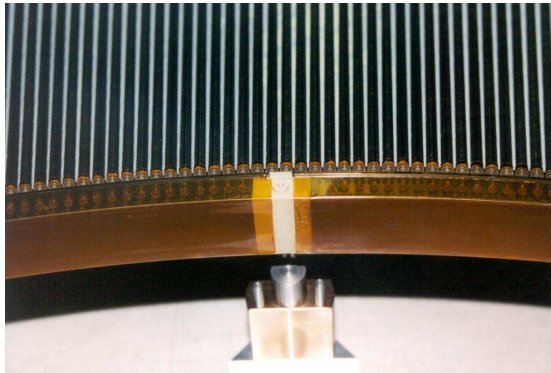


Figure 31. Two carters joined together with a cavalier. The straws with their end plugs inserted in the carbon fiber ring, can be seen through the Kapton®.



Figure 32. Completed eight plane A-wheel placed vertically onto transfer tooling.

cooling gas which enters each wheel at its inner radius, flows out along the straws and radiator foils before entering the next wheel.

The completed eight plane wheel A-type was placed vertically onto transfer tooling as shown in figure 32.

4.2.1 Quality control and wheel passport

In addition to the quality control and tests performed during assembly, all completed eight plane wheels were measured to ensure they met specifications and to prepare data for the so-called wheel passport. All critical points and specifications for the final evaluation of the quality of each wheel are summarized in appendix A table 11. The quality control tests listed in the upper part of table 11 were performed at the assembly sites during the assembly of four plane wheels. The tests listed in the lower part of table 11 were carried out on partially assembled eight plane wheels before they were shipped to CERN.

All wheel measurements and characteristics were recorded in the production database and all specifications were compared with the measurements obtained during production. The final information was included in the electronic passport of each wheel which is accessible through a web interface. Any wires found to be out of specification for a wheel had their anode disconnected from their signal line by unsoldering of the protection resistor since the design does not permit direct restringing of wires after ring 3 was installed.

4.3 Eight plane wheels acceptance tests at CERN

When a TRT end-cap wheel arrived at CERN it was subjected to a set of measurements, and acceptance tests [30] with similar procedures and tooling to those used at the assembly sites.

4.3.1 Measurement of wheel dimensions

Given the tight geometrical tolerances for the TRT, located between the SCT tracker and the Liquid Argon calorimeter, it is extremely important to comply with the dimensional envelopes. The



Figure 33. Complete eight plane wheel placed on a precision granite table at CERN for dimensional checking.

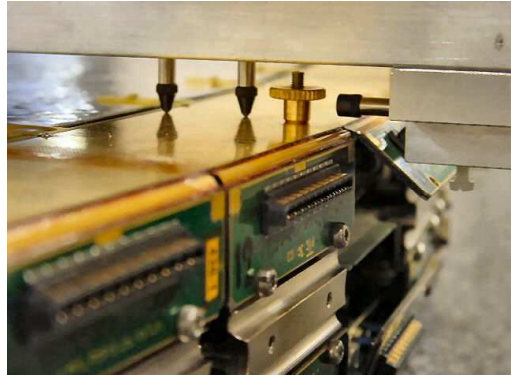


Figure 34. Digital measuring probes held by a rotary arm that are used to measure the dimensions of each eight plane wheel.

required envelope precision for the production and assembly of an end-cap wheel is of the order of 0.4 mm. All critical dimensions of the end-cap wheels were checked and compared to the specifications. These specifications include inner and outer radii and thickness. The outer radius, inner radius and thickness of the wheels, measured at 64 points at various azimuthally angles, are required to satisfy the requirements listed into table 11.

WEB reference holes were also checked during the dimensional tests — a 2.86 mm diameter rod has to pass through all pairs of reference holes in the active WEBs of eight plane wheels of both types A and B. Additionally, the same rod has to pass through at least two pairs of holes per WEB and through the corresponding reference holes of the assembly table.

Figure 33 shows an assembled eight-plane wheel installed on a $7 \mu\text{m}$ precision $2 \text{ m} \times 2 \text{ m}$ granite table for dimensional checking at CERN. The measuring device consists of a rotary arm holding digital measuring probes (figure 34) and a reference plate that allows calibration of the measurements. The measuring probes are capacitive sensors with a range of $\pm 10 \text{ mm}$ and a least count of $1 \mu\text{m}$. A data acquisition program is used to read out the sensors and store data on a portable PC for the further processing. The measured data were also stored in the acceptance data base [31].

4.3.2 Measurement of wire tension

Because wire tension is critical for the stability of straw operation, tension has to be controlled after delivery of the wheels to the CERN. The set-up used to measure wire tension at CERN is shown in figure 35. The same method that was used to measure wire tension at the wheel assembly sites was used at CERN (see section 4).

The loss of wire tension from production sites to CERN can be caused by several reasons among which are real slippage of the wire inside crimping pin, not fully inserted HV plugs which finally self slipped or self moved to the final place under the tension of the wire, measuring error during the wheel assembly and so forth.

Major attention was paid to wires which showed a tension loss of more than 5 grams. These cases were carefully investigated during data analysis. Since wheels assembly quality was high and the tension also was controlled during the assembly only a few anode wires out of 245,760 were disconnected due to tension problems.

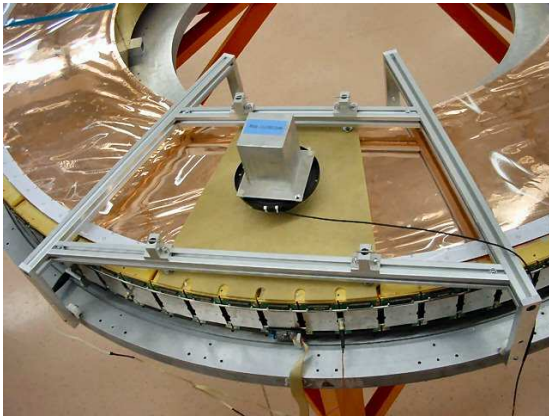


Figure 35. Wire tension setup showing the loud speaker resting on an epoxy-fibreglass plate to transmit vibrations to the wheel structure. Read-out electronics is connected to a cell of 32 straws.



Figure 36. High voltage test stand with several end-cap wheels under high voltage.

The distribution of the measured wire tensions for all wheels is shown in figure 37. The mean measured tension value is equal 67.9 grams and its RMS value is about 3.1 grams. The tension was required to be bigger than 50 grams and less 80 grams. Out of the 245,760 wires tested, 30 wires (0.012%) were found to be less than 50 grams and 153 wires (0.062%) more than 80 grams, i.e. outside specifications. The maximum wire tension was found to be 127 grams. As a limit of elastic deformation was measured at 150 grams while rupture occurs around 220 grams it was decided not to disconnect wires whose tension exceed the upper specification limit 80 grams.

The distribution of the difference between wire tensions measured at the assembly sites and that measured at CERN is shown in figure 38. A small systematic shift of ~ 1 gram is seen which probably is due to the slightly different method used to vibrate the wires. The repeatability of the wire tension measurements was also ~ 1 gram. The RMS of the difference distribution is about 2 grams. Out of the 245,760 wire tested, 308 wires (0.125%) were found have a tension loss from 5 to 10 grams, 67 wires (0.027%) from 10 to 20 grams and 23 wires (0.009%) more than 20 grams. All these cases were carefully investigated and the major cause turned out to be systematic errors in measurement at the production sites during wheel assembly. In the end only 45 wires (0.018%) were disconnected due to low tension of less than 50 grams or due to slippage.

4.3.3 Measurement of wheel gas tightness

The gas tightness test of assembled eight plane wheels was carried out by measuring the pressure drop in the closed detector gas volume filled with argon 20 mbar over atmosphere. The minimum test duration was 4 hours. Internal pressure, atmospheric pressure, and temperature were recorded during this test. The recorded temperature was used to correct the internal pressure. The leak rate (mbar/min/bar) was evaluated by fitting to the pressure drop trend. A wheel was considered valid for installation whenever the measured leak rate does not exceed 1 mbar/min/bar. The maximum value of leak rate for all measured wheels was found to be 0.53 mbar/min/bar.

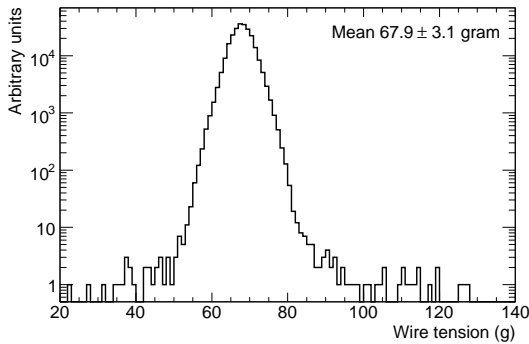


Figure 37. Wire tension distribution in all wheels as measured at CERN during the acceptance tests.

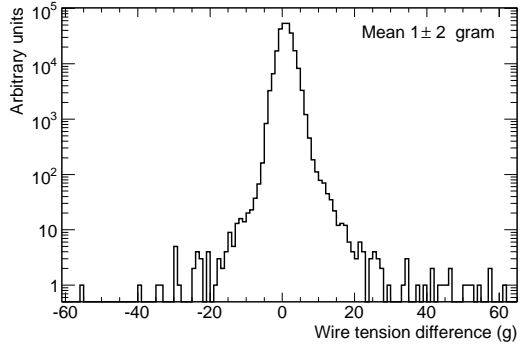


Figure 38. The distribution of the difference between wire tension measured at CERN and that measured at the production site shows no indication of significant tension losses.

4.3.4 Long term high voltage test

A short term high voltage stability test was carried out at the production sites during the assembly of the wheels as described at section 4. The goal of that test was to detect leakage currents, which arise mainly due to damage to the anode wire during installation into the straw, or shorts, mainly through the wheel support structure, since high-voltage was applied to the straw tubes while the wheel structure was at ground potential. At this stage most of the problems could be fixed by restringing the anode wires. The tests were performed in air before the closure of the gas manifolds and in CO₂ after completion of the wheel assembly.

The crucial test at CERN is a long term high voltage test which was intended to identify faulty channels (discharge or large leakage currents) in an active gas mixture of Ar-CO₂ 70/30 at a higher voltage (1550 V).

During the long term high voltage test the current and the number of trips were monitored. In cases of a large current or repeated trips, that particular high voltage channel was investigated to identify the faulty straw. If the problem in a particular channel (straw) prevented normal wheel operation, that channel was disconnected by removing the protection resistor. High voltage trips typically disappear after an initial test period, indicating some kind of cleaning process in the straw tubes. The elevated level of humidity in the laboratory sometimes caused high leakage currents from the straws to the rings — an effect which will be absent in the controlled environment of the running experiment.

The high voltage test specifications are listed in table 11. The acceptance specification was defined as: 6 days at 1480 V with the last 3 days at 1550 V without discharges. All assembled wheels successfully passed the long term high-voltage test. Several end-cap wheels placed onto the long term high voltage test at CERN are shown in figure 36.

4.3.5 Straw straightness measurement

Uniform gas gain along the straw tube is important for the safety of the detector and for optimal performance. The main reason for gas gain non-uniformity is some geometric deformation of the straw such as non-straightness or non-circularity or wire offset from the axis of the straw which

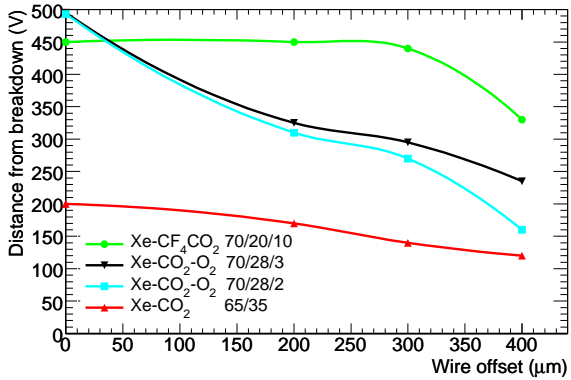


Figure 39. Voltage difference from the nominal TRT operating voltage to HV breakdown for different gas mixtures.

leads to a distortion of the electric field. For a wire offset of more than $400\text{ }\mu\text{m}$, the local increase of electric field substantially increase the gas gain. In this case, the rate of discharges and large amplitude signals increases significantly, making the straw very unstable under LHC running conditions.

Therefore the measurements of the gas gain along straw, or wire offset with respect to its nominal position within the straw, is the most critical test of the full set of acceptance criteria. The test also helps to check the operating efficiency of each straw, the high voltage distribution and any possible connectivity problems in the electronics signal read-out for each straw.

The measured margin before high voltage breakdown in different gas mixtures is shown in figure 39. The margin decreases from 500 V for a geometrically perfect straw to 250 V for a straw with $400\text{ }\mu\text{m}$ wire displacement for the TRT working gas mixture Xe-CO₂-O₂ 70/27/3. The margin before breakdown can be decreased by temperature variations inside the detector and by the flux of highly-ionizing particles. Therefore for safety reason the maximum allowable wire displacement was set to be $400\text{ }\mu\text{m}$.

One way to directly measure wire offset in the straw is by moving a narrow $\sim 50\text{ }\mu\text{m}$ X-ray beam across the straw and measuring the counting rate as a function of the position of the X-ray beam in the straw [32].

However, there is a simpler, but less precise and more indirect method to sense an imperfectly positioned wire. As any wire offset causes a disturbance of the electric field, it leads to increase of the signal amplitude and to distortion of the shape of the spectrum from a radioactive source such as ⁵⁵Fe. Figure 40 and 41 show two typical spectra with no wire offset and with offset $\sim 600\text{ }\mu\text{m}$. The main peak on the spectrum corresponds to the full absorption of the 5.9 keV photons in the straw which is irradiated by the ⁵⁵Fe source and the small peak on the left corresponds to the escape peak with an energy of 2.9 keV. The second figure clearly shows a distorted spectrum showing that there are at least two different regions of electric field (gain) within that straw [33].

The variation in gas gain and the increase in width of the measured spectrum were accurately measured as a function of wire displacement as seen in figure 42. Instead of the common FWHM (full width at half maximum) the full width at 20% of the maximum FW_{0.2} normalized to the peak position was measured in these tests.

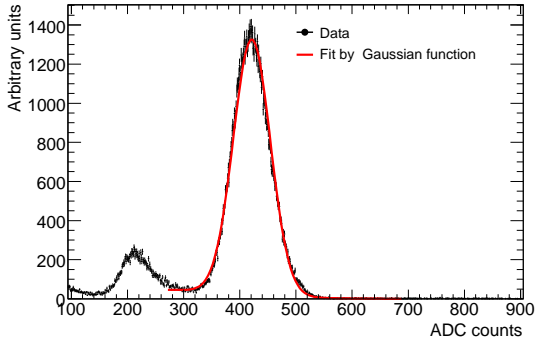


Figure 40. ^{55}Fe spectrum of a faultless straw showing the argon escape (left) and photo peak (right). A fit of the spectrum by a Gaussian distribution is shown.

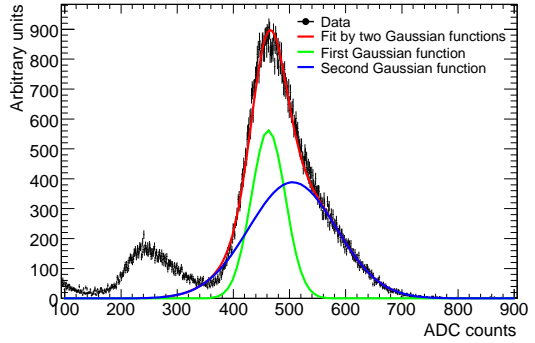


Figure 41. ^{55}Fe spectrum of a straw with wire offset $\sim 600 \mu\text{m}$. Fit of the spectrum by two Gaussian distribution is show.

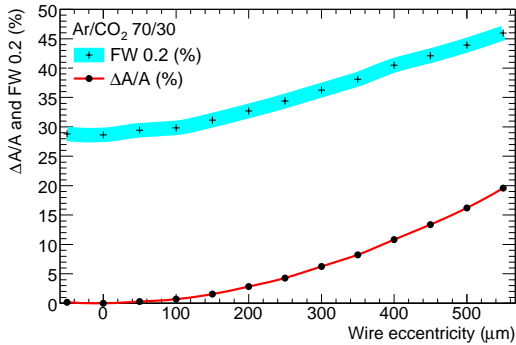


Figure 42. Measured relative change in gas gain and peak resolution against wire eccentricity. The systematic error on $\Delta A/A$ is order of 1%, and somewhat larger on the width ($\text{FW}_{0.2}$).

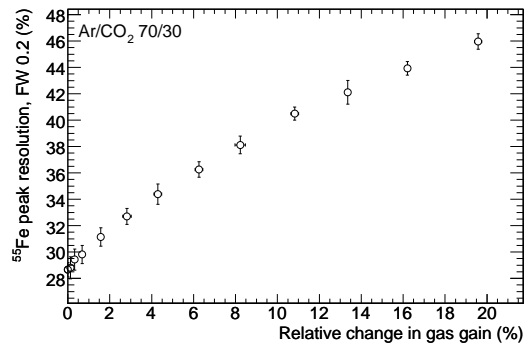


Figure 43. Correlation between changing gas gain and peak resolution.

A good correlation between the change in gas gain and peak width $\text{FW}_{0.2}$ with increasing wire eccentricity was found [34], so that bent straws can be clearly identified (figure 43). The wire offset, therefore, can be measured by observation of the gas gain and peak resolution variation along a straw using the calibration curve in figure 42.

For measuring the gain an automatized gain mapping setup - the Wheel Test Station (WTS) was employed. The WTS automatically scans each of the 3072 straws of a four plane wheel in one run and measures spectra at six positions along each straw using radioactive ^{55}Fe X-ray sources as shown in figure 44.

Only half of eight plane wheel, i.e. one four plane wheel, could be measured in one run because of the large absorption of the 5.9 keV X-ray photons from the ^{55}Fe X-ray source. To measure the other half of the eight plane wheel, it was reversed on the WTS for a second measurement of the second four plane wheel.

During this test the wheels are flushed with an Ar-CO₂ 70/30 gas mixture at the rate of 1 vol/h (corresponding to $\sim 40 \text{l/h}$ for an eight plane wheel).

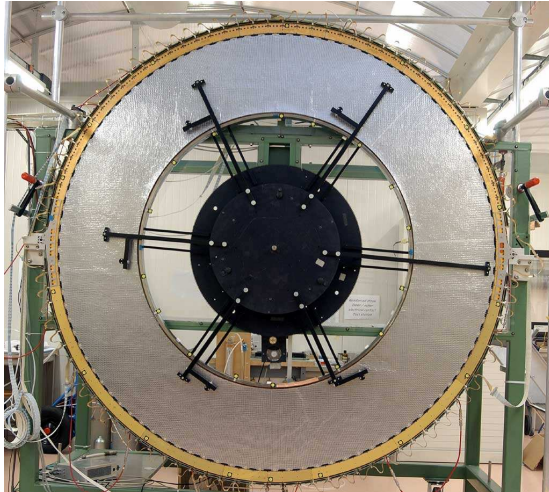


Figure 44. The eight plane wheel placed onto the Wheel Test Station (WTS) for straw straightness measurements. Six arms with ^{55}Fe X-ray source are seen.

To read out the signals the four plane wheel was equipped with 96 read-out boards each containing two GASSIPLEX chips [35, 36]. The GASSIPLEX is a 16-channel low noise ASIC for a very wide range of detector readout applications. A calibration pulse of stable amplitude can be injected into the electronic read-out chain in order to correct for pedestals and to monitor any baseline instabilities. Before the actual measurements, a channel-by-channel calibration at reduced high voltage was performed. The complete configuration of the electronic read-out (bar-codes of the boards, positions and connections) and the calibration data was stored in a database.

During the 40–50 hours run time a stepping motor automatically rotates the plate with six bars at different radii, each bar holding an ^{55}Fe source. At each step the six ^{55}Fe sources expose a group of straws at different radial positions. After a full turn of the plate six spectra of each of the 3072 straws were recorded as were reference spectra from a nearby straw to compensate for any temperature fluctuations. This compensation is especially important as the acquisition time between two points along the straw is around 7 hours — more than enough time for significant changes of temperature or atmospheric pressure.

By the end of the run for each four plane wheel the 18432 straw spectra (six per straw) and their corresponding 9216 calibration spectra for reference straws are recorded.

In an on-line analysis, each spectrum, including the calibration spectrum, was fit to a Gaussian to define mean and standard deviation of the photo peak. The mean value of the amplitude of the signal is proportional to the gas gain in the straw. The measured amplitudes were normalized to the corresponding amplitudes of the reference straw, i.e $A = A_{\text{meas}}/A_{\text{ref}}$.

The gas gain variation along the straw was finally calculated as the difference between the largest and the smallest normalized amplitude, divided by the smallest normalized amplitude, i.e. $\Delta A/A = (A_{\text{max}} - A_{\text{min}})/A_{\text{min}}$. The spectra, fit results and the gas gain variation were stored in the database for the further off-line processing. All straws with a gas gain variation more than 9% are flagged for later detailed off-line analysis.

The following figures 45, 46, 47, 48 show so called straw profiles, i.e. dependence of normal-

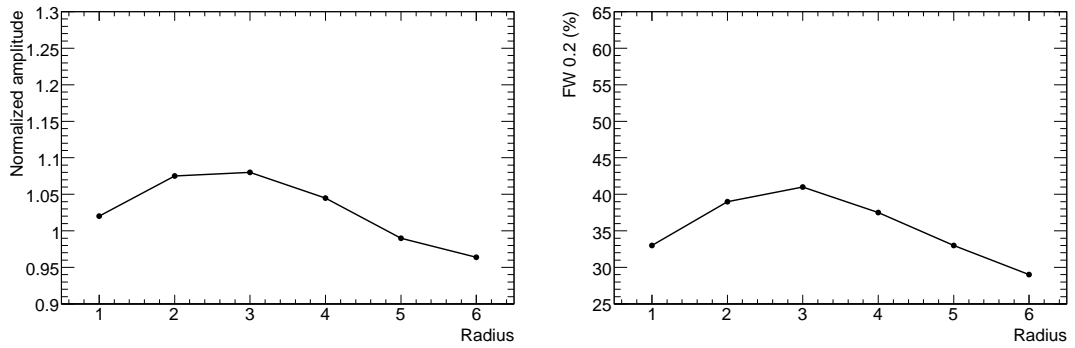


Figure 45. Dependence of normalized amplitude (left) and resolution FW_{0.2} (right) for each point of irradiation along the straw for the case of a bent straw. Point 1 corresponds to the outer radius of the wheel.

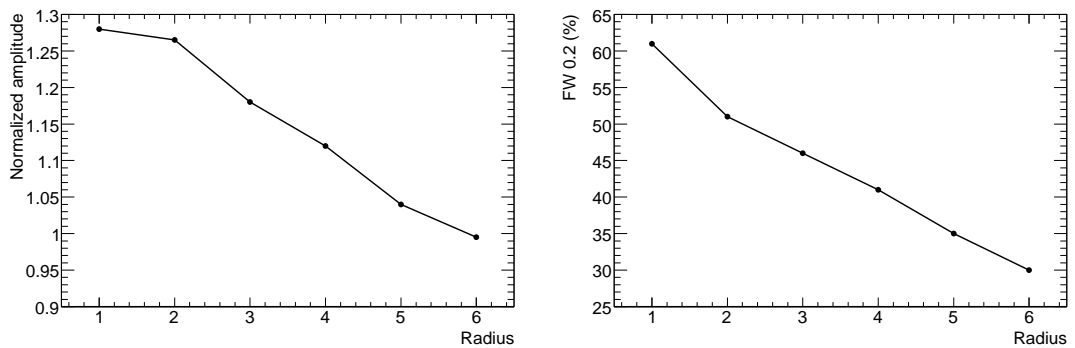


Figure 46. Dependence of normalized amplitude (left) and resolution FW_{0.2} (right) for the irradiation positions along the straw for the case of a "squeezed" straw. Point 1 corresponds to the outer wheel radius. Unlike the bent straw case, the maximum amplitude is located at the outer radius. Changes in amplitude and resolution are higher than for bent straws.

ized amplitude and full width of the peak at the level of 20% of maximum amplitude normalized to peak position, FW_{0.2}, for irradiation positions along the straw. These figures illustrate some well recognized signatures of anomalous straws which were found during the off-line analysis.

Figure 45 shows the straw profile for a "classical" bent straw. The increase of amplitude and the degradation of resolution in the middle of a bent straw is typical because the wire is centered by crimping pins at the ends of the straw and has the maximum offset with respect to the cathode in the middle of the bent straw. In some cases improperly stretched radiator foils produced a bend in the straw because the space between the straw layers was tightly filled by radiator foils and any "ridges" will cause a violation of the tolerance on the overall thickness of radiator foils.

Figure 46 illustrates a so-called "squeezed" straw — always with an amplitude rise at the outer end of the straw. This effect is caused by an error in the insertion of a straw tube into the outer insulation socket which has a four special grooves to accommodate the four C-fiber reinforcement filaments glued to the straw surface. If the C-fiber filaments do not match up with the special grooves in the insulation socket there is a non-circular deformation of the straw tube at the outer radius of the wheel which results in an increase of amplitude and degradation of resolution at the outer radius.

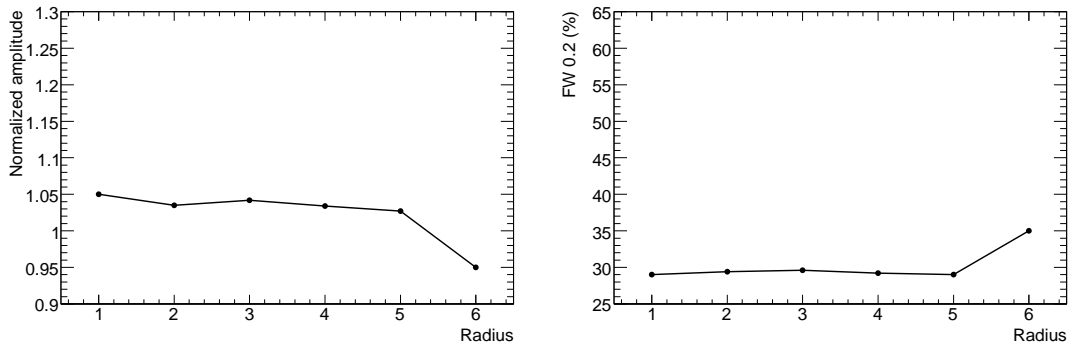


Figure 47. Dependence of normalized amplitude (left) and resolution FW_{0.2} (right) for the irradiation position along the straw for the case of straw with a “edge effect”. Point 1 corresponds to the outer wheel radius. The spectrum at point 6, which correspond to inner radius, has a very low counting rate compared to a normal straw. The reason is that the attenuation of the X-rays is greater at that point due to excess glue on the straw.

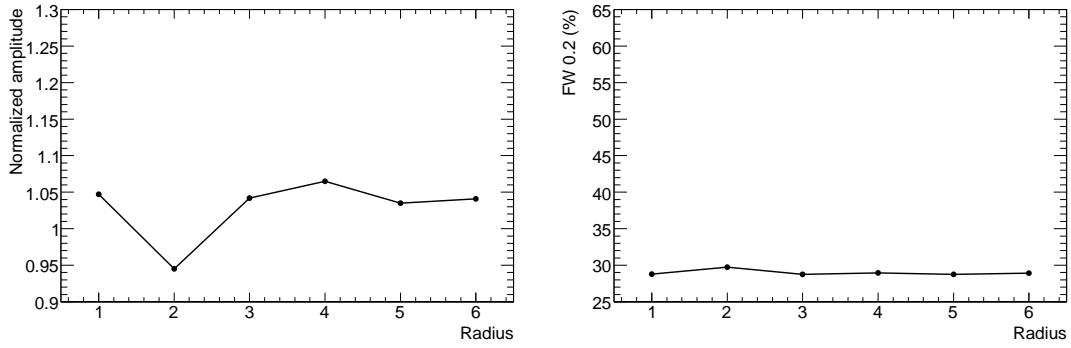


Figure 48. Dependence of normalized amplitude (left) and resolution FW_{0.2} (right) for the irradiation position along the straw in the not clearly defined case. Point 1 corresponds to the outer wheel radius. The local degradation of resolution and drop of amplitude at point 2 could be due to locally polluted wire, or a locally aged wire, or a local variation of the wire diameter.

The next two cases are rather rare. In the case shown in figure 47 we have the so-called “edge effect” which always occurs at the inner radius of the wheel and is accompanied by a spectrum with very poor statistics, i.e. counting rate is much less than for a normal straw. Visual inspection of those straws shows an excess of glue at the inner straw socket which increases the absorption of X-rays photons.

The explanation for the behavior demonstrated in the last case shown in figure 48 is not clear and probably would require visual inspection of the wire. The drop of amplitude and increase of spectrum width is observed in a small region along the straw. This case was carefully investigated by scanning the region in 1 mm steps with a collimated ⁵⁵Fe source. The size of anomaly was found to be about ~ 5 mm. There are three possible explanations of such behavior — wire pollution by dust or a local variation in the wire diameter or local aging of the wire.

The limit for wire displacement was chosen to be 400 μm and the criteria for disconnecting a straw was defined as combination of gas gain variation $\Delta A/A > 9\%$ and full width FW_{0.2} $> 35\%$.

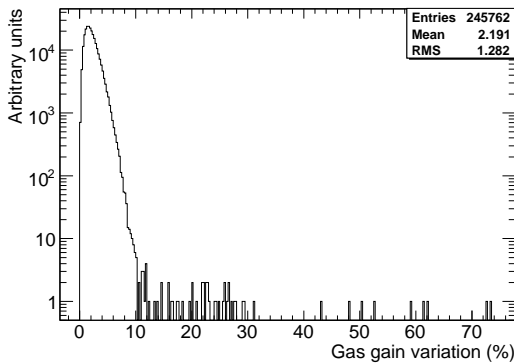


Figure 49. Distribution of the gas gain variation in all wheels as measured at CERN during the acceptance tests.

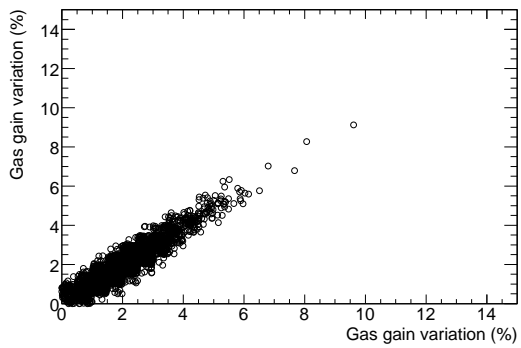


Figure 50. Correlation between gas gain variation measurements for the same wheel at CERN taken on month apart.

Table 9. List of the reasons for disconnecting a wire in both A and B type wheels.

Reason for wire disconnect	A-wheels		B-wheels		A and B wheels	
	Num.of wires	%	Num.of wires	%	Num.of wires	%
Tension	3	0.002	42	0.043	45	0.018
HV problem	16	0.011	4	0.004	20	0.008
Connectivity	84	0.057	89	0.091	173	0.070
Straw deformation	51	0.035	15	0.027	66	0.027
Total	154	0.104	150	0.153	304	0.124

The cases shown in figures 47, 48 were never considered as candidates for disconnection because these straws can operate normally and show no signs of instability.

The distribution of gas gain variation for all wheels is shown in figure 49. The mean measured gas gain variation is equal 2.2% and its RMS value is about 1.3%. Out of the 245,760 wire tested, 104 wires (0.042%) were found to have gas gain variations greater than 9%. After a careful analysis only 66 wires (0.027%) were disconnected due to straw deformations.

The reproducibility of the gas gain variation measurements is better than 1%, thanks in particular to careful control and monitoring of environmental conditions and this reproducibility is shown in figure 50, which plots the correlation between two measurements of the gas gain variation for the same wheel at CERN over a time interval of one month.

All straws which did not meet the acceptance criteria were disconnected from the signal chain for safety reason. In summary, only 304 straws (0.124%) out of more than 245,760 tested straws were disconnected for any reason. Table 9 summarizes the various causes for disconnecting a straw in both A and B type wheels.

The results of all acceptance tests were stored in the acceptance database and summarized in electronic end-cap wheel passports. The acceptance team prepared a Quality Report for each wheel. These reports were discussed in a Quality Circle and straws were disconnected only on the basis of a decision by the Quality Circle. Since the wheel assembly process continued in parallel with the testing of assembled wheels at CERN, the measurements of wire eccentricities and analysis of the

measured data helped to uncover problems at the assembly sites and correct those problems in the ongoing assembly.

The overall goal of assembling the TRT end-cap with less than 1% dead channels [1] was successfully achieved.

5. The end-cap group

5.1 Overview on the design of an end-cap group

On both sides of the intersection point there is a group of A-type wheels and a group of B-type wheels with the A-type wheels being closer to the interaction point in both cases. In principle, the groups of the same type of wheels are identical. Between each B-type eight-plane wheel there is a heat exchanger that cools the straw-cooling CO₂ gas. In the case of the A-type wheels, the heat exchanger is located between blocks of two eight-plane wheels.

At the end of each group there is a carbon fibre reinforced plastic membrane. These membranes are 10 mm thick. They have an outer diameter of 2100 mm and an inner diameter of 1246 mm. At their inner radius the two membranes are connected by a 1 mm thick fibre glass reinforced plastic cylinder. During the assembly the outer surface of the group is made gas-tight so that this surface, the two end membranes and the inner cylinder form a closed volume. CO₂ enters through one of the end membranes, passes through the series of wheels being successively heated by the straws and cooled by the heat exchangers and leaves through the other end membrane.

The group is held together by 92 stainless steel tie rods of 2.5 mm diameter that pass through the holes in the active and passive webs of each four-plane wheel and through corresponding holes in the end membranes. A force of some 216 N is applied to each tie rod. Each tie rod has a spring at one end in order to ensure that it is subjected to a quasi-constant tension. The end membranes are further connected on the outer radius by two titanium girders. Special attention had to be given to the design of the girders and end membranes in order to reduce the deformation of the finished group to acceptable levels. The weight of individual eight-plane wheels is taken by the girders. Four elastic feet attached to a titanium girder transmit the weight of the whole group to the two girders, the so-called squirrel cage girders, sliding on the support rails. The squirrel cage consists of a 5 rings which supports 32 cable trays and two girders to support detector on the support rails. It serves also as a Faraday cage.

5.2 Assembly and integration

5.2.1 Mechanical assembly

The groups were assembled with the cylinder axis in the vertical position. Although this entails a mechanism to subsequently turn the group through 90 degrees, the additional complexity of this operation was greatly outweighed by the convenience of having the wheels horizontal during assembly.

The assembly tooling is illustrated in figure 51. The main support structure consists of six vertical columns. Three of these columns (the so-called 'precision columns'), arranged in an equilateral triangle, have plates attached with precision drilled reference holes equal to the distance between successive eight-plane wheels. Corresponding reference holes in each of the three plates



Figure 51. TRT end-cap assembly tooling for the wheels stacking into one group.



Figure 52. Rotation of the completed TRT wheel B-type stack before final integration to the TRT end-cap.

lie in a horizontal plane. Brackets were attached to the plates and indexed to one of the holes. During assembly a new element was always added at the same height with respect to the ground. Before adding the next element the partially assembled group was lowered the appropriate distance by moving the support brackets to the appropriate reference hole.

To begin the assembly a thick support ring, calculated to have an acceptably small deformation under the weight of the full group, was placed on the brackets. The first assembly operation was to fix the end membrane, via shims, onto the support ring. Although the reference holes in the precision columns ultimately ensure that the support ring was horizontal, any element that was placed on the partially assembled stack was free to move in the horizontal plane. In order to constrain this liberty a 'reference triangle' was attached with brackets to the upper portion of the precision columns and above the partially assembled group. Before adding another element to the stack the reference triangle must be centred with respect to the end membrane. In order to do this the end membrane has 3 flat plates screwed to it and referenced to the circumferential holes. Each plate has a radial slot that extends beyond the outer rim of the end membrane; the axes of the three slots were 120 degrees apart. The reference triangle has three holes drilled in its corners. Using a system based on precision spirit levels the reference triangle was moved in a horizontal plane until the centre of each of these holes was vertically above the axis of the corresponding slot on the end membrane. Near each of the holes just described there was a long vertical hole into which an accurate 3 mm pin can be inserted. These pins were inserted into the corresponding holes in the active WEBs in the eight-plane wheels (or, during the last operation, into similar holes in the closing end membrane). This indexing operation was carried out with the item to be added supported on thin shims. The item was then temporarily supported on three thin blades, the shims were extracted and the item lowered onto the partially finished group.

Adjacent eight-plane wheels never touch each other directly. They were either separated by the plates that carry the heat exchangers, or (in the case of the A-type group) by spacer plates. In both cases the plates were made from 7.5 mm thick fibre glass. Both sets of plates have holes corresponding to those in the active and passive webs, but since these devices demand no great positioning precision, the holes were of larger than those in the webs. Both the heat exchanger plates and the spacer plates were glued onto the wheels during the assembly phase. In this way small deviations from parallelism between the wheels can be compensated.

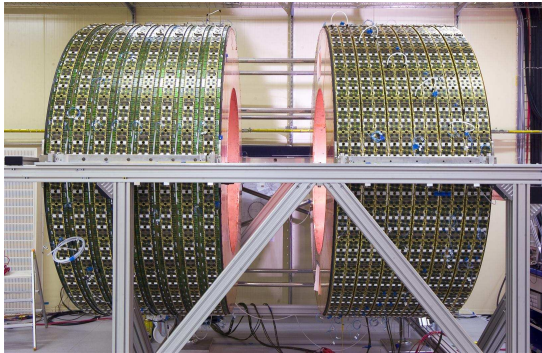


Figure 53. The A and B groups of wheels placed to the assembly trolley.

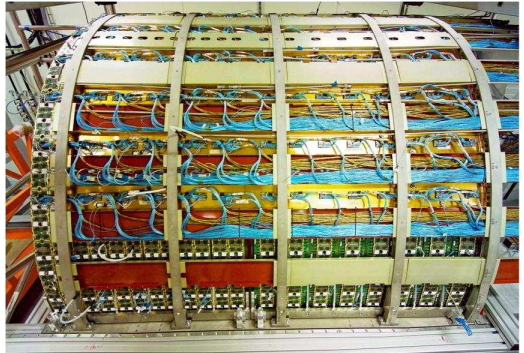


Figure 54. The TRT end-cap with mounted five squirrel cage rings and 32 cable trays.

Although the group was held together firmly by the series of tie rods, it was felt prudent to add another system to prevent catastrophic slipping of the wheels with respect to one another. In addition, a system was required to prevent lateral movement of the elements during assembly. The heat exchanger plates and the spacer plates were drilled with a series of 12 mm diameter holes. After the lateral position of the wheel has been fixed, 11.9 mm diameter disks were glued to the eight-plane wheel. A simple jig ensures that these discs lie directly above the corresponding holes. After the glue has set the upper item was raised and the jigs removed. Provision was made to insert a neoprene sealing joint between the plate and the upper element and this element was then lowered into its final, locked, position.

The last stacking operation for each group was the positioning of the upper end membrane. After this the tie-rods were inserted through the holes in the webs, their associated strings were added and the rods were tensioned to the correct force. In the case of the A-type group, the gaps between those eight-plane wheels that were cooled as a pair were sealed using an insulating band. The final assembly operations were the insertion of the inner cylinder (this serves the dual roles of protection and shielding) and the attachment of the girders connecting the two end membranes (these girders were equipped with feet that will support the group after it has been turned).

A major part of the assembly, which we have not described in detail here, consists of the installation of the many cooling pipes (both for the active gas and the straws), the temperature probes and the electronics. In addition the group was continuously monitored to ensure that the dimensions remain within tolerance.

The next operation was to turn the group through 90 degrees so that its axis was horizontal (figure 52). To do this a supplementary tooling was attached to the lower support ring. Critical elements of this tooling were two deep beams, initially vertical, onto which the turning axes were bolted. (The turning axes were positioned at the centre of gravity of the group.) Rails were attached to the beams; after turning to the horizontal position these become the temporary support rails for the group. Two additional short pillars were added to the stacking tooling between pairs of opposite columns. Using the hydraulic system the vertical group was lowered until the turning axles locate in veees placed at the summit of the newly added pillars. After removing those elements of the stacking apparatus that could impede the operation, the group was turned carefully to the horizontal position and slid onto a transfer chariot for transport to the integration area.

From the transfer trolley, the two groups of wheels were moved to the assembly trolley by rolling on top of the squirrel cage girders aligned on the support rails (figure 53). The load of each group was then transferred from the rolling supports to the final elastic posts. The two groups were precisely positioned going through several robotic arm measurements and an optical survey. The integration of each TRT end-cap proceeds now with the mounting of the CO₂ flow control valves and the implementation of the Faraday cage between the inner cylinders and the end carbon membranes. The five squirrel cage rings were assembled around the two groups and made ready to receive the 32 cable trays (figure 54). These contain the pre-assembled and tested cables with part of the cooling pipe system already embedded. The cable trays were inserted one by one, and connections to the front-end electronic board made and tested.

The next phase sees the cooling and active gas systems completed and tested. The complex piping system covers the electronics cooling, the heat exchanger for the CO₂ ventilation gas cooling, the active gas feeding and return and the CO₂ ventilation lines together with the pressure monitoring system. The reliability of the connections was verified through systematic testing at each step. Connectivity checks for the electronics proceed in parallel with the leak tightness test of every sector. Once a sector was validated it was then closed by the outer Faraday cage panels. These were made of copper-beryllium pre-shaped foils forming the outer EC shielding by connecting on each sector the five rings. All services were ended at the PPF1 connection panels where test devices were plugged in. After the last mechanical alignment a set of survey measurements confirms the correct pre-positioning of the end-cap with respect to the final installation requirements in the cavern. The Inner Detector installation trolley was connected and precisely aligned to the assembly jig. The end-cap was slid on by use of a pushing device and was made ready for the insertion of the SCT end-cap (figure 55).

5.2.2 Mounting and testing of the on-detector electronics

This section briefly describes the installation of the TRT end-cap front-end electronics, the tests performed on and the results achieved after the completion of the installation of the detector in the ATLAS experimental cavern. The TRT end-cap front-end electronics have been described elsewhere [37] in detail, and only a short description is given here.

The avalanche signal produced in the detection gas by particles crossing the straws is read out by the eight channel ASDBLR chip (Analog Shaper, Discriminator, and Base Line Restorer). The ASDBLR receives and shapes the signal, canceling out the long xenon ion tail, and then compares the signal to the low (for tracking purposes) and high (for detecting transition radiation for particle identification purposes) thresholds. The output of the ASDBLR is received and digitized by the DTMROC (Digital Time Measurement and Read Out Controller). The information corresponding to the low threshold is sampled every 3.125 ns, while that corresponding to the high threshold is sampled every 25 ns, or once per bunch crossing. When an event is requested via the receipt of a level-1 trigger, the DTMROC sends out three bunch crossings, worth of data.

The TRT end-cap electronics front-end boards were sent to CERN from the Niels Bohr Institute [39] where they were tested in a stand-alone test bench. The tests were designed to check the complete functionality of each board and its corresponding chips. All of the registers of each DTMROC were exercised, a fine timing scan was run to check the command lines, and a noise scan was run with the internal test pulse firing to characterize the analog performance and identify dead or

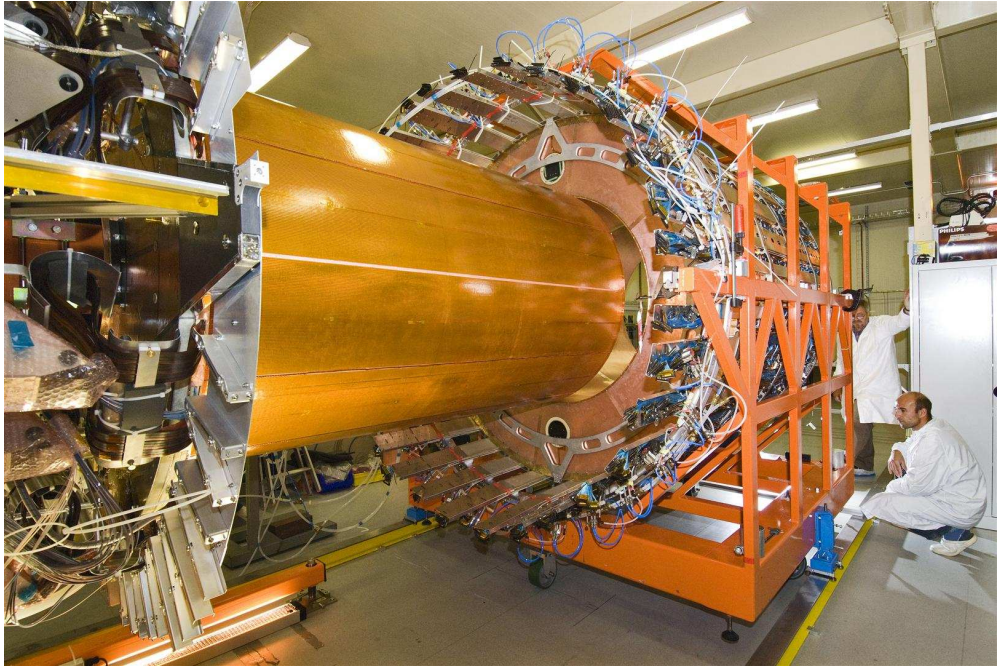


Figure 55. TRT end-cap detector placed on the Inner Detector installation trolley for integration with SCT end-cap.

problematic channels. The data from these tests were stored in a database, and a web interface was developed for tracking board shipments and repair histories. These tests were repeated at CERN to check that all the channels were operational and that no damage occurred during transport.

The installation and the tests of the front-end electronics on the detector followed a two step procedure — a first set of tests was made off-detector, to get a proper reference for comparison. Then, the front-end electronics were installed on the detector where a last set of tests was made to detect any potential detector, connectivity or electronics failures. The same hardware readout and test software were used in both cases, and the details of the tests have been described in [38].

The integration of the electronics on the detector started by closing the rigid part of the WEB [37]. The WEB was fixed to the front-end electronics cooling structure inside the wheel with non-magnetic screws. The alignment of the Fujitsu connectors, which received the ASDBLR, was checked during this operation with a plastic template. The analog ground planes were connected between two successive wheels with one 10 Ohm resistor per WEB. The side of the ASDBLR board in contact with the cooling plate was covered with a special foam to ensure a good thermal connection. The ASDBLR board was fixed to the cooling plate with a single centered metallic standoff. The DTMROC “triplet” was then connected on the top of the ASDBLR. Each “triplet” serves three ASDBLR boards, and is constructed as three separated DTMROC boards connected together using flexible jumpers, to follow the wheel curvature. The “triplet” was fixed to the ASDBLR with screws made of PEEK [23]. The digital ground planes between the three DTMROC boards forming the triplet were connected together by inserting a gold plated spring under each of the four flexible jumpers.

The tests performed on the electronics, before and after installation on the detector, comprised:

- A TTC (Timing, Trigger and Command) fine delay scan, where the clock and the TTC signals are delayed by 1 ns steps, scanning the complete 25 ns range of the LHC clock. The quality of data transmission is checked at each point.
- A data fine delay scan, where the clock and the data signals are delayed by 1 ns steps, scanning the complete 25 ns range of the LHC clock. The quality of data transmission is checked at each point.
- A noise scan over the full range of the 8 bit low-level threshold with a step of one, taking 250 events per scan point.
- A built in test pulse scan (2 fC pulse) over the full range of the low-level threshold with a step of one, taking 250 events per step.
- A built in test pulse scan (30 fC pulse) over the full range of the high-level threshold with a step of one, taking 250 events per step.

After the installation of the electronics on the detector, two additional tests were done:

- A scan of the DTMROC's built-in voltage and temperature monitoring functionality.
- A run using the accumulate mode of the DTMROC chip at one set of thresholds (the DAC values were set to 120 for the tracking threshold (~ 300 eV) and 45 for the transition radiation threshold (~ 1.2 keV)), with 50 events at each of the different gating time windows. This last test uses the DTMROC's feature, which allows the high threshold bit, after it has been set, to stay high until the relevant bit register has been cleared by software. This makes it possible to measure the dark current (background rate of high threshold hits) and to check the connection of the straws to the high voltage distribution.

These tests were repeated after the installation of all the services. For this purpose, prototypes of the TTC, Data and Low Voltage patch panels [37] were used to power and read-back a complete TRT end-cap φ slice (20 front-end boards) at a time. All the previous tests took place in a surface building, in the assembly area, and were repeated again after the installation of the detector in the ATLAS experimental cavern. In this last case, the final versions of the patch panels and of the back-end TTC board were used. For the back-end ROD (Read Out Driver) board, a prototype was used. All the results of each of these tests are stored in a MySQL-based database and are retrievable for further analysis.

Note that some channels which showed very low noise but passed the dark current test were registered in the list of suspicious channels, though they are probably properly connected and perfectly functional. Before the installation of the services, the suspicious channels were all checked by measuring the capacitance and the diode voltage of the corresponding channel on the detector (see figure 56 for a schematic view of the connection between the TRT end-cap and its front-end electronics), but such a check was not possible after the installation of the services and the closing of the Faraday shield. All channels which showed anomalous behavior after the installation of the services were also registered as potentially problematic. As a consequence, the numbers given below are certainly a worst case estimate. For the two end-caps, 535 (933) of these suspicious channels were found during the assembly on the surface (see [40] for details) on the 1st (2nd) end-cap,

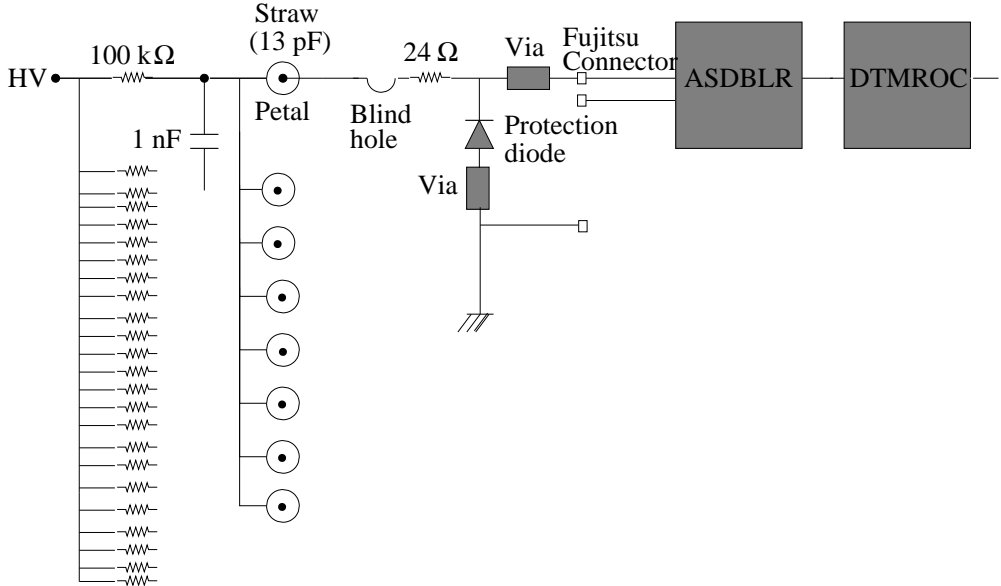


Figure 56. Schematic view of the connection between the TRT end-cap and its front-end electronics.

corresponding to 0.6% of the 245,760 channels. After the installation in the experimental cavern, some channels were lost due to low voltage or high voltage shorts or breakdowns, and also due to some failing DTMROC chips. The high voltage has not yet been tested with either the dark current method nor with real particles in the end-caps, and results given are only based on capacitance measurements. Tests in the cavern add 32 (dead DTMROC chips), 1728 (low voltage failures), 768 (high voltage failures) and 192 (unknown failure) bad channels to the previous numbers. In summary, 98.3% of the two TRT end-caps is perfectly functional.

The main sources of failures are:

- For 64.2%, low voltage or high voltage failures after installation in the experimental cavern.
- For 21.8%, the suspicion is on the detector itself: bad vias on the WEB or a disconnect from the high voltage distribution (blown fuses, broken or disconnected straws).
- for 7.2%, mechanical disconnection of the straw during assembly (known before the tests and registered in the wheel acceptance database).
- for 6.8%, the front-end electronics itself (channels or chips which failed after the installation of the services in a position where the front-end electronics were no longer accessible for replacement).

5.2.3 Mounting and testing of monitoring sensors

To ensure safe operation of the end-caps, temperature sensors were placed at various positions on the detectors. Platinum resistance thermometers (PT1000) with a sensitivity of $3.85 \Omega/\text{Kelvin}$ were used for the sensors.

The sensors serve five major purposes:

- Sensors to measure the temperature of the liquid cooling the front-end electronics: to measure the temperature of the cooling liquid, the two cooling pipes on an eight plane wheel are each equipped with one sensor at the inlet and one sensor at the outlet, in total there are 40 (56) sensors per end-cap group.
- Sensors to monitor the temperatures of the straws: to achieve a stable detector operation, it is necessary to supply the Gas Gain Stabilisation System [41] with the temperatures of the detecting elements. There is no possibility to measure the temperatures inside the straws. However, simulations of the thermal behaviour have shown that the temperature conditions of the CO₂ straw cooling gas in the volume of the heat exchangers are directly proportional to the average temperature inside the straws. Thus there are four sensors installed for each cooling gas outlet to the heat exchangers and additional four sensors in the path of the CO₂ straw cooling gas close behind the heat exchangers. The sensors are positioned on the top and bottom, left and right, spaced by 90°. As there is a heat exchanger between each group of two type A eight plane wheels (5 heat exchangers in the type A group) and one between each type B eight plane (in total 7 heat exchangers in the type B group) in total 96 sensors per end-cap are mounted.
- Sensors to measure the temperature of the cooling liquid inside the heat exchangers: on each inlet and outlet pipe of a heat exchanger, temperature sensors are mounted. As there is a heat exchanger between each group of two type A eight plane wheels (in total 5 heat exchangers in the type A group) and one between each type B eight plane wheel (in total 7 heat exchangers in the type B group), per end-cap in total 24 sensors are installed.
- Temperature sensors on the mechanical structure: to monitor the temperature of the mechanical structure, sensors are placed on the outer carbon fiber ring (ring 3). For each eight plane wheel, four sensors are mounted, on the top, bottom, left and right, spaced by 90°, thus 80 sensors per end-cap.
- Additional environmental sensors: on the top and bottom, left and right, spaced by 90°, at the input and output of the CO₂ straw cooling gas of each type A and type B group, temperature sensors were installed. An additional four sensors are mounted between two type B wheels (B4, B5) and between two type A wheels (A3, A4). The sensors are positioned at smaller wheel radii, at radial position of about 2/3 of the wheels outer radius. In total there are 24 environmental sensors per end-cap.

6. Services

6.1 Distribution of active gas

One of the requirement of the normal operation of the TRT end-cap is the uniform circulation of active gas through each straw. The active gas for the straw drift tubes is Xe(70%), CO₂(27%), O₂(3%). This gas is supplied through two lines in the first of the two four planes in an eight plane wheel, and exits from the neighboring four plane. The two outer carbon fibre rings, the passive and active WEBS form a gas manifold that distributes the gas in R-φ. The straw end plugs have

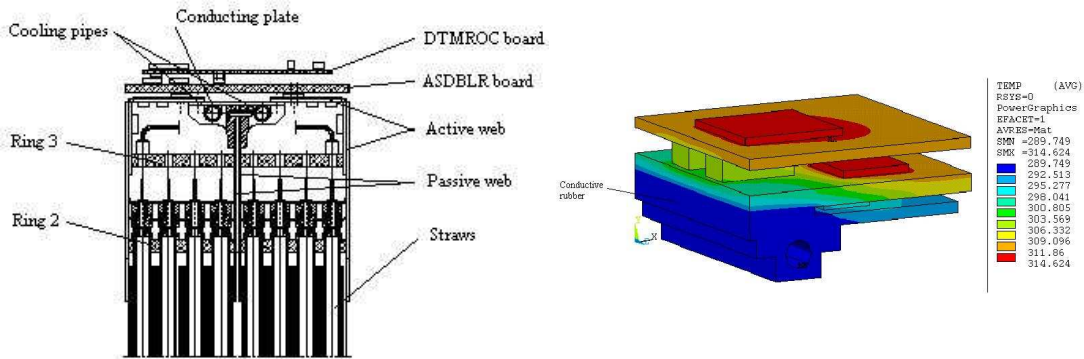


Figure 57. Cross-section of an eight plane module at the outer radius. The cooling pipes runs in $R\varphi$ and are connected to the electronics through an aluminum plate.

Figure 58. Temperature distribution with additional thermal connection inserted.

sufficient impedance to guarantee a uniform distribution of the active gas. At the inner radius the gas is collected into an inner gas manifold before entering to the second four plane wheel at the inner radius and finally recuperated at the outer radius. The target gas flow is one volume exchange per hour or 5 cm^3 per straw and hour. The exit gas is recovered, cleaned and recirculated.

6.2 Electronics cooling

The electronics as well as the straws themselves need to have heat removed from the detector area. This is accomplished by circulating a coolant (Fluorinert™ [42]), C_6F_{14} which has a high boiling point of 56°C at atmospheric pressure. The liquid circulates from a central cooling plant to four distribution racks located near the detector and then through the detector modules. For the design and testing of the cooling system a front-end electronics power dissipation of $100 \text{ mW}/\text{channel}$ in order to give a good safety margin. This heat is removed by conduction from the under surface of the ASDBLR board coupled via thermal foam to an aluminum conducting plate attached to the cooling tubes. The Fluorinert™ runs in the cooling pipes in $R\varphi$ which are bolted to the aluminum cooling plates as shown in figure 57. In order to cool the straws themselves which can produce⁷ up to $28 \text{ mW}/\text{m}$ of straw, CO_2 cooling in combination with heat exchangers are used (see section 6.3). The heat exchangers are also cooled with the Fluorinert™ in the same circuit as the electronics. The nominal entrance temperature of the fluid is 15°C , and the fluid flow is set to have a maximum temperature increase of less than 8°C at the return. A cross-section of an eight plane module with cooling pipes and front-end electronics is shown in figure 57. Each eight plane module has two cooling circuits with two inlet and two outlet pipes covering 180 degrees. Calculations have been performed to verify the temperature gradients between the cooling pipes and the heat sources on the boards (see figure 58). The specification for leak tightness was $<100 \text{ l/year}$ for the entire manifold and plumbing system. The leak rate in any cooling circuit in a single wheel was too low to measure and it was expected that the major loss would be in connections between the cooling circuits and the pipe work from the detector to the cooling racks and in the cooling racks themselves. The volume of plumbing distribution lines from the racks in the cavern to the detector is more than 400 l .

⁷For counting rate of 17 MHz at the design luminosity $L = 10^{34} \text{ cm}^2\text{s}^{-1}$

6.3 Straw cooling

6.3.1 Requirements

The 2440 W of heat estimated to be dissipated in the TRT end-cap straws at the nominal LHC luminosity of $10^{34} \text{ cm}^{-2}\text{s}^{-1}$ has to be removed from the detector by a flow of dry CO₂ around the straws in order to guarantee temperatures in the detector between 20°C and 30°C and to ensure end-caps thermal neutrality. Higher detector temperatures would limit detector performance as the drift time would change and thermal expansion of the anode wires would decrease their mechanical tension and hence their position accuracy [43]. For the LHC nominal luminosity, this temperature range determines a total flow of $150 \text{ m}^3\text{h}^{-1}$ in the closed loop ventilation system [44, 2]; $50 \text{ m}^3\text{h}^{-1}$ for A-type wheels and $25 \text{ m}^3\text{h}^{-1}$ for B-type wheels. Due to mechanical limitations, the TRT has to be kept at atmospheric pressure with $\pm 5.5 \text{ mbar(g)}$ accuracy, which is small compared to the 1000 mbar pressure drop over the whole CO₂ cooling system. High flows compared to small detector volumes ($50 \text{ m}^3\text{h}^{-1}$ through 0.8 m^3 for A-type wheels) give small reaction times; for instance, 5.5 mbars are reached in 317 ms in a worst case regulation failure where a valve closes completely in the detector outlet line.

In addition to closed loop cooling, a continuous CO₂ renewal of $3 \text{ m}^3\text{h}^{-1}$ is needed to purge polluting gases. This minimizes Transition Radiation (TR) absorption in the cooling gas by any xenon possibly leaking from the active gas mixture (Xe(70%), CO₂(27%) and O₂(3%)) as well as anode wire etching by water from moist air leaking into the low pressure lines. The detector relative pressure should also remain positive to minimize pollution by N₂ [45] or silicones from the neighboring sub-detectors. The specifications are N₂ < 1%, Xe < 0.1% and water < 500 ppm. Silicones have to be avoided at a ppm level inside the straws as they induce premature aging of the anode wire [46]. Oils have to be avoided too because they increase gas permeability of the straw wall.

6.3.2 System tests and validation

Due to the possibly catastrophic consequences of a pressure increase in the detector, tests were carried out on a full scale prototype [44]. The prototype included a pump module, gas renewal, distribution rack 1 connected to a detector mock-up of 900 liters, a simplified version of distribution rack 2 connected to a dummy volume of 450 liters and a small 20 liter buffer volume to model the ID enclosure. These tests showed that minimizing the impact of active regulating components and decoupling parallel regulation loops (either in time or amplitude) allowed successful and robust pressure regulation between 0 and 3 mbar(g) in the detector. Despite turbulent flow regimes in all pipes, the only significant perturbations of the system once stabilized were environmental changes like pressure and temperature that happen on time scales larger than the regulation period with amplitudes easily compensated for by the regulation. Long runs over 24 hours showed stable regulation between 0 and 1 mbar(g). Harmful pressure excursions in the detector mock-up were only observed with double component failures including at least one passive valve blocked in closed position on the detector. Such a passive valve was tested in a cycling test with one stroke every 5 seconds without breaking and without excessive wear over 110,000 cycles. Knowing that the valve might only open fully a few times per year, such a double component failure has a very low probability.

The efficient regulation achieved with the prototype was also obtained on the final system after commissioning.

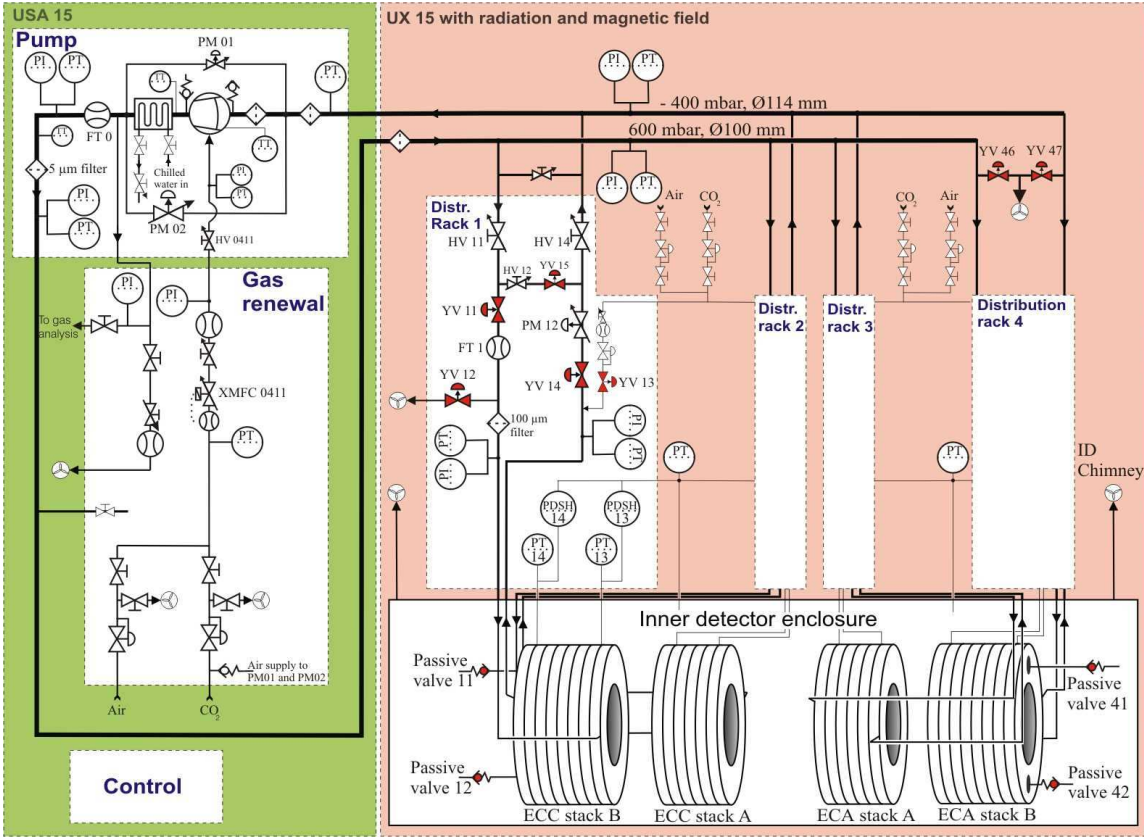


Figure 59. The CO₂ cooling system layout can be split into modules: control, pump, gas renewal, distribution racks, detector.

6.3.3 The pump module

The pump module (figure 59) ensures CO₂ circulation and smooth flow changes to allow accurate pressure regulation by the distribution racks. The flow can be increased either by ramping up the pump frequency or by closing the bypass valves PM01 and PM02 (two valves of different sizes act complementarily to ensure accuracy over the whole range). A water cooled heat exchanger removes heat gained by the CO₂ during polytropic compression in the dry rotary lobes compressor.

6.3.4 The gas renewal module

The gas renewal module provides CO₂ to the system with a mass flow controller tunable up to 6 m³h⁻¹. An exhaust line allows the loss of system gas. In the simplest regulation mode this exhaust line is closed and the input flow is set to a constant 3 m³h⁻¹ and any excess gas is lost through the four detector over-pressure passive valves thus maintaining the amount of gas in the system constant and ensuring CO₂ renewal. Safer transitions between run and stop states were achieved with a balanced system for which the total CO₂ mass at atmospheric pressure is almost equal to the total CO₂ mass in running conditions; a CO₂ displacement occurs during flow ramp-up from the low pressure side to the high pressure side of the system. Nominal pressures in both send and return lines therefore depend on their volumes.

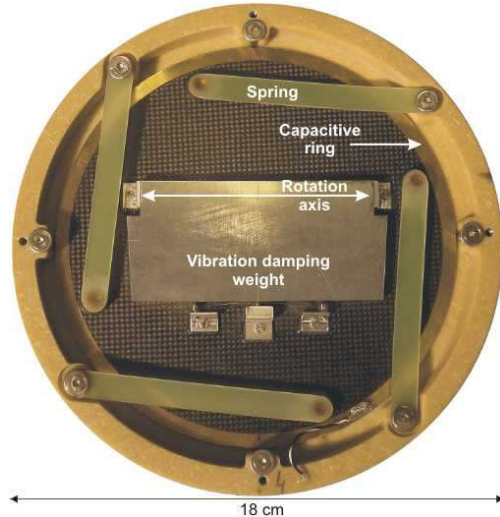


Figure 60. Passive valve mounted on the detector. Glass fiber springs have been tuned to apply the proper closing force on a carbon fiber disk. A vibration damping aluminum weight hangs on a rotation axis. Two rings mounted on the moving disc and on the support allow capacitive position measurement. The ensemble is 1 cm thick.

6.3.5 The distribution racks

For each stack of wheels, a distribution rack allows setting the CO₂ flow and regulating the pressure in the detector. The relative flow in each line is set manually by tuning the distribution line impedance (HV#1 and HV#4). The detector outlet pressure (PT#4) is read by a PID loop that corrects the set-point of the pneumatic valves PM#2. In addition, fast ON-OFF pneumatic safety valves (YV##) allow the system to quickly isolate the detector from the rest of the system in the case of regulation failure. The combination of a DN100 mm wafer type pneumatic valve with a smaller pneumatic pilot valve and a radiation and magnetic field resistant piezo valve allows a stroke of 120 ms. Once in the fail safe position (YV# 1..# 5 respectively closed, open, open, closed and open) the detector is purged by a CO₂ flow entering through YV13 and exhausting through YV12 connected to a ventilation inlet at about -0.1 mbar(g). This ensures that the detector is always purged with CO₂. Valves YV46 and YV47 allow for the purging of the main distribution line before reconnection to the detector. The opening of bypass valve YV#5 ensures low perturbations in the other distribution lines and gentler flow ramp-down in the main loop in case of a system shut-down. In addition to detector pressure monitoring by the Programmable Logic Controller (PLC) with pressure transmitters (PT#3 and PT#4), mechanical differential pressure switches were added for redundant shut down of the safety valves in case of over-pressure (PDSH#3) and under-pressure (PDSH#4) via a hardwired interlock. For the simplest regulation scheme where the gas renewal module outlet is closed, one of the regulation valves, e.g. PM32, receives a constant set point and passive valve 31 acts as a back pressure control valve, thus regulating the amount of CO₂ in the whole system.

6.3.6 Installation on detector and control racks

Due to radiation (10 Mrad in 10 years), magnetic field (2 T) and space limitations, only passive

components are installed on the detector for this cooling system. CO₂ enters each detector stack at room temperature (20°C) through a distribution manifold [47] and is cooled on its way through the wheels by several plate heat exchangers in which liquid C₆F₁₄ flows. This creates a CO₂ pressure drop of up to 1 mbar for A-type wheels with nominal flow between the stack inlet and outlet volumes. The same monophase cooling system using liquid C₆F₁₄ ensures cooling of both TRT electronics and CO₂ heat exchangers inside end-caps wheels [37]. The CO₂ temperature is monitored by PT1000 sensors placed both before and after C₆F₁₄ heat exchangers. These temperatures are not used by the CO₂ cooling system. Cooling CO₂ volumes in the detector are 0.8 m³ for A-stack and 1.5 m³ for B-stack. Over-pressure and under-pressure passive valves (figure 60) have been mounted on each stack close to the CO₂ outlet. Their flow versus pressure characteristic is such that the nominal CO₂ cooling flow can be safely diverted through one of them (e.g. in case of a blockage either in the inlet or in the outlet line).

The control racks contain a PLC with input and output interfaces to the various parts of the system. The PLC contains all operational and regulation algorithms and communicates with the PVSS [48] supervisory layer.

7. Summary of weights and material distribution

Determination of the as-built material distributions and the weights of the TRT end-cap wheels is an important part of the detector description. The assembled end-cap C was weighed in September, 2006 using three precision sensors and the total mass was 1118 ± 12 kg after removing the additional weight of some temporarily installed parts and adding of some missing parts. The same measurement was made in November, 2006 for end-cap A and its total weight is 1120 ± 12 kg.

The stacks of the TRT wheels may be divided into different functional volumes (figure 61): inner volume, active region, outer volume, membranes, services, and, for stack type B, end ring. The inner volume includes all inactive parts of the detector: pins, carbon-fiber rings, gas etc. which are closer to the beam axis than the active region of the straws. The outer volume is defined like the inner one but includes the outer inactive parts of the detector and also the front-end electronics. The active volume is defined as the active part of the straws. The weights of these volumes are listed in table 10. A detailed estimate of the total weight of an end-cap stack was made using input from the technicians and engineers who designed and built the detector. Wherever possible the measured weight of components have been used but in some cases component weights have had to be calculated or estimated from the technical drawings. Complete results of this study are available at [8].

The contribution of different materials to the radiation and nuclear interaction lengths are calculated in order to understand degradation of the spatial resolution of the detector which is formally divided into functional volumes, as shown in figure 61 (for details see [8]). Two different directions are used for the calculations: parallel to the z axis crossing the active volume of the entire end-cap, as well as perpendicular to the z axis crossing volumes of stack A and stack B. The results of these calculations are shown in table 10. Total contributions of end-caps also summarized there. For the simulation of the detector a simplified description was used with mixtures of three different materials whose combination gives correct values for the weights and of the radiation and interaction lengths.

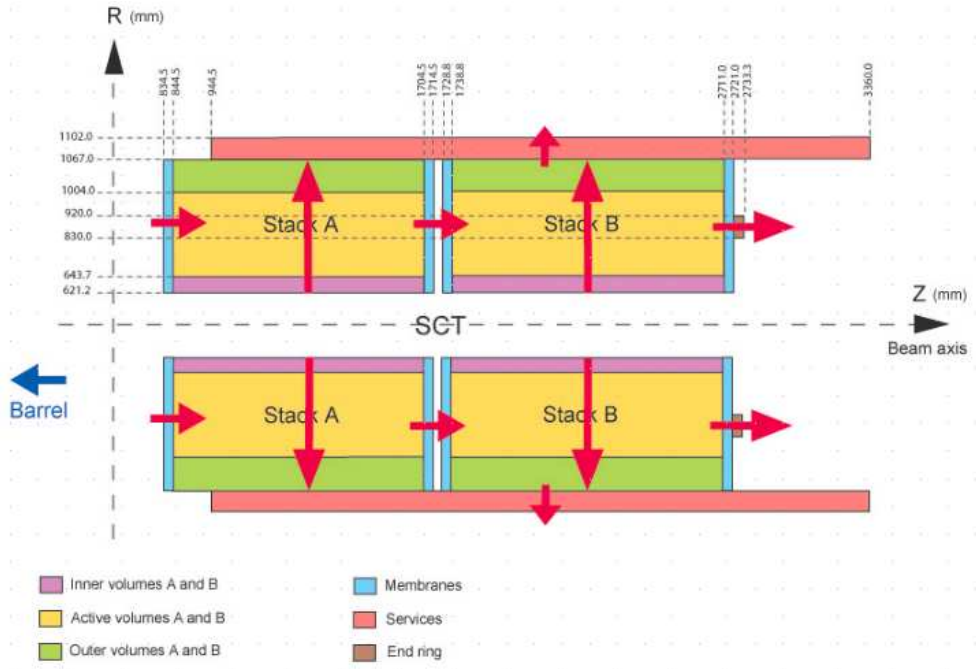


Figure 61. Definition and orientation of the TRT end-cap volumes.

8. Performance of end-cap modules at beam tests

In order to validate the TRT end-cap design, a dedicated prototype representing one sector of a 16 plane wheel (384 straws) was constructed and tested during a series of test beam runs (figure 62). All final electrical connections were implemented and prototypes of final electronics boards were attached to the detector.

This prototype was installed in the H8 line of the CERN SPS and tested during LHC structured beam tests (40 MHz bunch structure) in May 2003.

In order to obtain a precise particle trajectory and identify the beam particle auxiliary detectors were used. A three plane silicon telescope with intrinsic resolution of $10\text{ }\mu\text{m}$ was used as external tracking to define the beam trajectory. Measurements with TRT modules were carried out using the baseline mixture $70\%\text{Xe}+27\%\text{CO}_2+3\%\text{O}_2$. Figure 63 shows an event display for the test beam prototype. Straw noise occupancy as a function of the electronics threshold is shown in figure 64. One sees that at the threshold of 250 eV straw noise occupancy is about 2% which satisfies the TDR specification [2].

One of the most important detector performance parameters is spatial resolution defined as the sigma of the distribution of the track residuals. For the test beam, the track residuals were found by comparing the space points measured using TRT drift-time information with the particle positions projected from the silicon-telescope measurement. Another critical parameter is the TRT end-cap efficiency which is defined as the probability for finding a drift-time measurement hit within a $\pm 2.5\sigma$ window from the beam particle track. Figures 65 and 66 show the behaviour of these parameters as a function of ASDBLR threshold. One sees a spatial resolution of about $120\text{ }\mu\text{m}$ and an efficiency of about 85% is reached at the nominal operating threshold of $250\text{-}300\text{ eV}$. The above

		perpendicular to the z axis					parallel to the z axis, crossing active volume				
Volume name	Weight (kg)	T (cm)	X ₀ (g/cm ²)	X/X ₀ (%)	λ ₀ (g/cm ²)	λ/λ ₀ (%)	T (cm)	X ₀ (g/cm ²)	X/X ₀ (%)	λ ₀ (g/cm ²)	λ/λ ₀ (%)
Inner volume A	38	2.25	24.94	4.49	94.70	1.18	-	-	-	-	-
Active region A	92	36.03	36.23	5.78	84.11	2.49	85.71	36.23	6.87	84.11	2.96
Outer volume A	270	6.3	24.15	20.30	96.49	5.08	-	-	-	-	-
Membranes (×2)	12	-	-	-	-	-	1.0	35.71	1.43	88.04	0.58
Stack of A wheels	424	44.6	27.84	30.57	98.81	8.75	86.71	36.12	9.73	84.90	4.12
Inner volume B	33	2.25	24.83	3.55	91.82	0.96	-	-	-	-	-
Active region B	104	36.03	36.38	5.73	81.42	2.56	96.96	36.38	7.71	81.42	3.44
Outer volume B	276	6.3	24.68	17.99	93.45	4.75	-	-	-	-	-
Membranes (×2)	12	-	-	-	-	-	1.0	35.71	1.43	88.04	0.58
Stack of B wheels	437	44.6	28.44	27.27	95.24	8.27	97.6	36.25	10.57	82.59	4.60
Services	219	0.3	18.87	7.09	112.17	1.19	-	-	-	-	-
End-ring	12	-	-	-	-	-	1.23	24.01	10.01	106.40	2.26
Squirrel cage	36	0.8	24.01	8.99	106.40	2.03	-	-	-	-	-
Total end-cap	1128±10	-	-	-	-	-	185.5	35.36	62.11	37.33	54.36
Stack A	424	45.7	23.11	96.76	99.49	20.40	-	-	-	-	-
Stack B	437	45.7	23.46	93.46	97.08	19.92	-	-	-	-	-
measured											
end-cap A	1120±12										
end-cap C	1118±12										

Table 10. Weights, thicknesses, radiation, and interaction lengths of the end-cap volumes. The values are given for two scenarios: parallel to the z axis crossing the active volume of the entire end-cap, as well as perpendicular to the z axis crossing volumes of stack A and stack B.

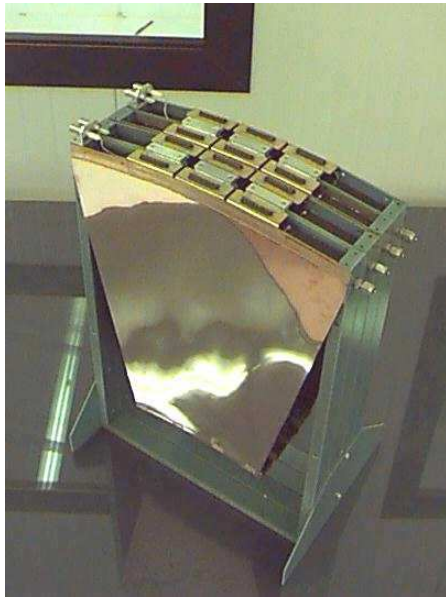


Figure 62. The TRT end-cap test beam prototype representing one sector of the 16 plane wheel.

results are consistent with the expected TRT end-cap performance in the ATLAS Inner Detector at the LHC.

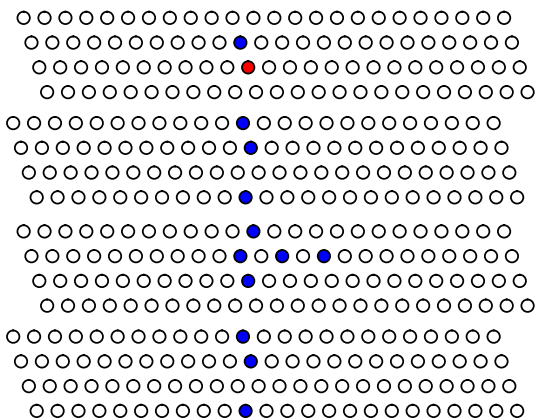


Figure 63. Test beam event display shows the track of a particle crossing the TRT end-cap test beam prototype. Open circled straws without signal. Filled circles show straws crossed by beam particle. The blue circles indicate that the straw has a low level signal while red circles show that a transition radiation photon was detected (high threshold signal).

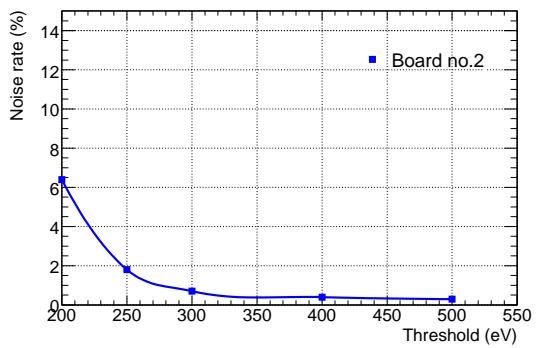


Figure 64. Straw noise occupancy as a function of the low-level threshold on the analogue chip.

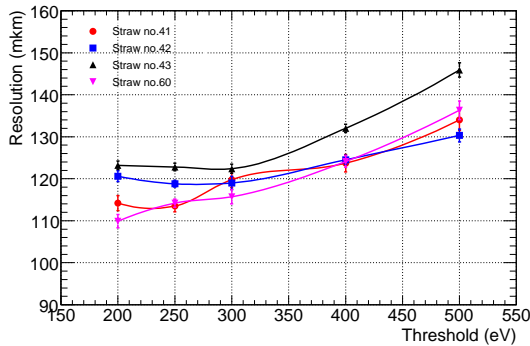


Figure 65. The TRT end-cap spatial resolution as a function of the low-level threshold on the analogue chip.

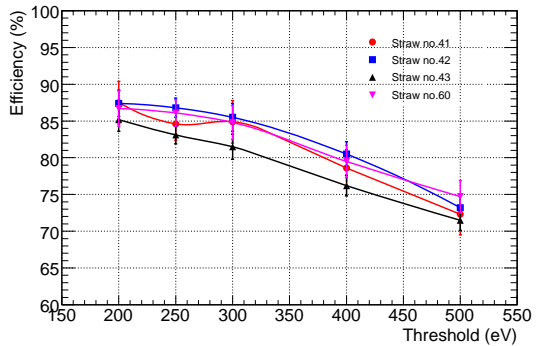


Figure 66. The TRT end-cap efficiency defined as the probability for finding a drift-time measurement hit within a $\pm 2.5 \sigma$ window from the beam particle track as a function of the low-level threshold on the analogue chip.

9. Summary and conclusion

We have successfully completed the design, construction and integration of the end-caps of the ATLAS Transition Radiation Detector. Studies of the design of the detector started in 1990 with the RD-6 Collaboration and a series of beam tests and prototype modules resulted in an optimised design minimising the amount of insensitive detector material. A series of novel techniques and materials, carefully tested to survive the harsh and demanding environment of the LHC, were applied and used. Over the period 1998 to 2004, a total of 25 eight plane wheels of type A and 17

eight plane wheels of type B were constructed at two production sites within the Russian Federation. This construction required about 50 person-years of work. The wheels were extensively tested and the best 24 type A and 16 type B wheels were selected for assembly at CERN into the two end-caps of the Transition Radiation Tracker. The integration of the wheels together with the associated services, the supplies for active gas, electronics and straw cooling, the distribution of the high voltage, the on-detector electronics and the monitoring sensors into end-cap groups was completed in 2007. Institutes and teams from CERN, Denmark, Poland, Russian Federation, Sweden, Turkey and the United States of America contributed to this effort. The detectors are now installed in the ATLAS experimental cavern and the final tests and sign-off demonstrated that more than 98.3 % of the 245,760 detecting elements and electronics channels are operational and waiting to record tracks originating from the first LHC collisions.

Acknowledgments

The research described in this publication was partly supported by following funding agencies: the European Union (DGXII), the International Science Foundation, the Danish Natural Science Research Council, the Swedish Research Council, the Knut and Alice Wallenberg Foundation, the Ministry of Science and Higher Education, Poland, the International Science and Technology Centre, the Civil Research and Development Foundation and grants from the U.S. Department of Energy and the U.S. National Science Foundation, the Natural Science and Engineering Research Council of Canada, the Ministry of Education and Science of the Russian Federation, Russian Federal Agency of Science and Innovations, the Academy of Sciences of the Russian Federation, the International Association for the Promotion of Cooperation with Scientists from the new Independent States of the former Soviet Union, the Turkish Atomic Energy Authority.

A. Summary of acceptance tests

Test of 4-plane wheels	Test goal	Specification	Typical value
Gas tightness (mbar/min/bar)	Check gas-tightness of non-wired straws fixed to the support rings	<1.0 at 20 mbar overpressure of Ar	0.4
HV current (nA)	Check quality of the HV connections of the straws without wires	50 per 32 straws at 2500 V on air	<10
Wire tension (g)	Check wire tension	55 < T < 80	68
HV current (nA)	Measure dark current of the straws with wires	50 per 32 straws at 1800 V on air	<30
Gas tightness (mbar/min/bar)	Check gas-tightness of completed 4-plane wheel	<1.0 at 20 mbar overpressure of Ar	0.2
HV current (nA) per	Measure dark current of the completed 4-plane wheel and identify faulty channels (discharges or large leakage)	50 per 32 straws at 1800 V on CO ₂	<45

Dimensional check: Thickness, wheel A (mm) Thickness, wheel B (mm) Minimum radius (mm)	Check conformity of the thicknesses; checking of the inner radius	33.0 ± 0.2 56.5 ± 0.2 < 623.75	33.05 56.3 624.5
Wire offset (μm)		< 300	< 200
Test of 8-plane wheel	Test goal	Specification	Typical value
Gas tightness (mbar/min/bar)	Check gas-tightness of completed 8-plane wheel	< 1.0 at 20 mbar overpressure of Ar	0.2
CO_2 tightness (mbar/min)	Check gas-tightness of CO_2 envelope for completed 8-plane wheel	1 for 5 mbar overpressure of CO_2	< 0.5
HV (nA)	Check that no faulty channels (discharges or large leakage) during 15 days	150 for 192 straws at 1480 V on Ar/ CO_2 70/30 gas mixture	
HV (nA)	Check that no faulty channels (discharges or large leakage) during 7 days for increased HV	150 for 192 straws at 1550 V on Ar/ CO_2 70/30 gas mixture	
Wire tension (g)		$50 < T < 80$	68
Wire tension loss (g)		< 15	< 3
Wire offset (μm)		< 400	< 200
Dimensional checks: Thickness, wheel A (mm) Thickness, wheel B (mm) Minimum radius (mm)	Check of conformity of the thicknesses; checking of the inner radius	67.05 ± 0.4 114.0 ± 0.4 623.35	67.2 113.8 623.9
Tests during stacking 16-plane A and 8-plane B	Test goal	Specification	Typical value
HV training	Identify faulty channels (discharges or large leakage)	No faulty channels or Ar- CO_2 gas mixture	
Dimensional	Intrinsic part of the stacking process		
Gas tightness test (mbar/min/bar)	Check gas leakage of 16-plane wheel	< 1.0 at 20 mbar overpressure of Ar	
Fluid C_6F_{14} tightness test (cm^3/min)	Check tightness of the cooling circuits (electronics and heat exchangers) and connections	$< 10^{-5}$ at 3 bar when circuits are filled up with gas or no pressure drop in 24 hours when circuits are filled with > 5 bar of fluid C_6F_{14}	
Electrical tests	Check of contacts and grounding		
Circulation tests	Verify the absence of vibrations or any other unexpected problem	Filling up all cooling circuits with C_6F_{14} at 1.5 times the nominal working pressure (5 bar)	
Thermal-sensors checks	Functionality and calibration test. Read out and calibrate all temperature (NTC and PT1000) sensors	All sensors working and calibrated in the adequate range	

FE electronics tests	Verify board functioning: grounding and shielding checks, noise levels, map of faulty channels	No grounding and shielding problems	
Thermal tests of FE and cooling	Check temperature range when cooling is on and power on FE boards is on		
CO ₂ flow test	Vibration, flow and pressure drop checks	No vibration, pressure and flow drops	
CO ₂ tightness test	Check tightness of the completed stack	<1 mbar/min at 5 mbar overpressure of Ar	
Cosmic rays	Check the stacks at working conditions with cosmic rays		
Tests on a completed end-cap			
Dimensional	Intrinsic part of the stacking process		
Gas tightness test (mbar/min/bar)	Check tightness of complete end-cap	<0.1 mbar/min at 20 mbar overpressure of Ar	
Fluid (C ₆ F ₁₄) tightness test		Check tightness of complete end-cap	
Thermal tests of FE/cooling			
Circulation tests	Check liquid circulation of complete end-cap		
Services checks			
System tests	Verify board performance noise, faulty channels, grounding and shielding		

Table 11: List of tests carried out during the wheels stacking process and on completed end-caps with their specification and obtained typical values.

B. Fact sheet

Item	Unit	Value
Straw		
diameter	mm	4±0.04
wall thickness	μm	70
wire diameter	μm	30
active gas mixture		Xe/CO ₂ /O ₂ , 70/27/3
high-voltage	V	1530
gas gain		2.5×10 ⁴
drift time	μm/ns	52
Total number of straws		245760
per end-cap		122880
A-wheels		73728
B-wheels		49152
per 8-plane wheel		6144
Straw layers per end-cap		160
A-wheels		96
B-wheels		64
Distance between layers		
A-wheels	mm	8
B-wheels	mm	15
Number of radiator foils		
A-wheels		12-17
B-wheels		21-32
Number of 8-plane wheels per end-cap		20
A-wheels		12
B-wheels		8
Weight		
end-cap A	kg	1120±12
end-cap C	kg	1118±12
Envelopes		
z _{min}	mm	822
z _{max}	mm	2739
R _{min}	mm	620
R _{max}	mm	1103
Active gas volume:		
8 plane wheel A-type	l	~16.1×2
8 plane wheel B-type	l	~17.8×2
Readout channels		245760

Continued on next page

Item	Unit	Value
Dead channels		4172 ⁸
after assembly:		
end-cap A		304
end-cap C		81
new after integration		223
end-cap A		1164 ⁹
end-cap C		454
new after installation in the pit		710
end-cap A		2704
end-cap C		1728
		976
Power supply		
High-Voltage lines		
per end-cap		640
per wheel type-A		32
per wheel type-B		32
Low-Voltage lines		
per end-cap		448
per wheel type-A		16
per wheel type-B		32
Read-out electronics		
ASDBLR		
per end-cap		15360
per wheel type-A		768
per wheel type-B		768
DTMROC		
per end-cap		7680
per wheel type-A		384
per wheel type-B		384
ROD		
per end-cap		32
Cooling system		
for straws		CO ₂
for electronics		C ₆ F ₁₄
Heat dissipation for one end-cap		
from straws	W	3360
from electronics	W	32040
Physics parameters		
Active volumes:		

Continued on next page

⁸Real number of dead channels can be obtained from data only.⁹The number extracted from noise test of the front-end electronic boards.

Item	Unit	Value
$ z_{\min} $	mm	847.8
$ z_{\max} $	mm	2709.6
R_{\min}	mm	643.7
R_{\max}	mm	1004.0
η region:		0.77-2.14
wheels A		0.77-1.70
wheels B		1.32-2.14
Space resolution		
at $L=10^{33} \text{ cm}^2\text{s}^{-1}$	μm	170
at $L=10^{34} \text{ cm}^2\text{s}^{-1}$	μm	200
Average hits number		22 - 36
Average TR hits number		
electron		5-10
pion		2
Maximum counting rate	MHz	$7\text{-}19 \text{ MHz}^{10}$

Table 12: Fact sheet.

References

- [1] ATLAS collaboration, *ATLAS Inner Detector technical design report. Vol. 1*, ATLAS-TDR-004, CERN-LHCC-97-016.
- [2] ATLAS collaboration, *ATLAS Inner Detector technical design report. Vol. 2*, ATLAS-TDR-005, CERN-LHCC-97-017.
- [3] ATLAS Pixel collaboration, *ATLAS Pixel Detector Electronics and Sensors*, 2008 JINST **3** P07007.
- [4] ATLAS SCT collaboration, A. Abdesselam et al., *The barrel modules of the ATLAS semiconductor tracker*, Nucl. Instrum. Meth. **A 568** (2006) 642.
- [5] A.J. Abdesselam et al., ATLAS SCT collaboration, *The ATLAS semiconductor tracker end-cap module*, Nucl. Instrum. Meth. **A 575** (2007) 353.
- [6] ATLAS TRT collaboration, E. Abat et al., *The ATLAS TRT Barrel*, 2008 JINST **3** P02014.
- [7] ATLAS collaboration, *ATLAS technical proposal for a general-purpose pp experiment at the Large Hadron Collider at CERN*, CERN-LHCC-94-43.
- [8] M. Goulette, *Update on the TRT end-cap material weight*, ATL-INDET-PUB-2007-001.
- [9] RD6 collaboration, *Systematic study of straw proportional tubes for the ATLAS Inner Detector*, ATL-INDET-93-018.
- [10] Petersburg Nuclear Physics Institute (PNPI), Russian Academy of Science, Gatchina, St.Petersburg, Russian Federation, <http://www.pnpi.spb.ru>.
- [11] Joint Institute for Nuclear Research (JINR), Dubna, Moscow Region, Russian Federation, <http://www.jinr.ru>.

¹⁰Depends on z position of the straw.

- [12] A. Romaniouk, *Choice of materials for the construction of the TRT*, ATL-INDET-98-211.
- [13] Mashinostroitel, Perm, Russian Federation, <http://pzmash.siteholder.ru>.
- [14] ATLAS TRT Collaboration, T. Akesson et al., *Study of straw proportional tubes for a transition radiation detector/tracker at LHC*, *Nucl. Instrum. Meth. A* **361** (1995) 440.
- [15] ATLAS TRT collaboration, E. Abat et al., *The ATLAS Transition Radiation Tracker (TRT) proportional drift tube: design and performance*, 2008 *JINST* **3** P02013.
- [16] Lamina Dielectrics Ltd Billingshurst, West Sussex, England.
- [17] PEI, Polyetherimide is an amorphous, amber-to-transparent thermoplastic with similar characteristics to PEEK's, <http://en.wikipedia.org/wiki/Polyetherimide>.
- [18] Ultem is a family of polyimide thermoplastic resins, of type amorphous polyetherimide, <http://en.wikipedia.org/wiki/Ultem>.
- [19] FR4, an abbreviation for Flame Retardant 4, is a type of material used for making a printed circuit board, <http://en.wikipedia.org/wiki/FR4>.
- [20] E. Onistchenko et al., *Research and development high voltage fuses for the transition radiation tracker in ATLAS experiment*, CERN EDMS ATL-IT-QN-0012.
- [21] H. Danielsson, *Estimated particle identification performance of the ATLAS Barrel TRT from beam studies on a barrel prototype*, ATL-INDET-97-187.
- [22] W. Funk, *A systematic study of the particle identification performance in the Transition Radiation Tracker (TRT) of ATLAS*, ATL-INDET-97-157.
- [23] PEEK, Polyetheretherketone, is a thermoplastic with extraordinary mechanical properties, <http://en.wikipedia.org/wiki/PEEK>.
- [24] F. Guarino, S. Ilie, A. Romaniouk, S. Soutchkov and F. Tartarelli, *Outgassing studies of the TRT materials for the TRT construction*, CERN EDMS ATL-IT-FN-0002.
- [25] ATLAS TRT collaboration, T. Akesson et al., *Ageing studies for the ATLAS Transition Radiation Tracker (TRT)*, *Nucl. Instrum. Meth. A* **515** (2003) 166.
- [26] M. Capeans-Garrido et al., ATLAS TRT Collaboration, *Recent ageing studies for the ATLAS Transition Radiation Detector*, *IEEE Trans. Nucl. Sci.* **51** (2004) 960.
- [27] ATLAS TRT collaboration, T. Akesson et al., *Aging effects in the ATLAS transition radiation tracker and gas filtration studies*, *IEEE Nuc. Sci. Symp. Med. Imag. Conf.* **2** (2005) 1185.
- [28] Yu.V. Gusakov, I.A. Zhukov, V.M. Lysan, V.V. Myalkovskii, A.F. Novgorodov and V.D. Peshekhonov, *Automated stand check of "B" type TRT ATLAS wheel straw detectors*, *Phys. Part. Nucl. Lett.* **3** (2006) 206.
- [29] PNPI TRT end-cap wheel production database, <http://atlas.pnpi.nw.ru/wf/new/wf.html>.
- [30] ATLAS TRT collaboration, P. Cwetanski et al., *Acceptance tests and criteria of the ATLAS transition radiation tracker*, *IEEE Trans. Nucl. Sci.* **52** (2005) 2911.
- [31] CERN TRT end-cap wheel acceptance database, <http://trt-wts.web.cern.ch/trt-wts/wf.html>.
- [32] ATLAS TRT collaboration, T. Akesson et al., *An alignment method for the ATLAS end-cap TRT detector using a narrow monochromatic X-ray beam*, *Nucl. Instrum. Meth. A* **463** (2001) 129.

- [33] P. Cwetanski, A. Romanouk and V. Sosnovtsev, *Studies of wire offset effects on gas gain in the ATLAS TRT straw chamber*, ATL-INDET-2000-016.
- [34] P. Cwetanski, *Straw performance studies and quality assurance for the ATLAS transition radiation tracker*, Report Series in Physics, HU-P-D133, Helsinki, Yliopistopaino (2006), <http://ethesis.helsinki.fi/julkaisut/mat/fysik/vk/cwetanski/>.
- [35] J.C. Santiard and K. Marent, *The GASSIPLEX0.7-2 Integrated Front-End Analog Processor for the HMPID and Muon Tracker of ALICE*, CERN-ALI-99-23.
- [36] J.C. Santiard, et al., *Gassiplex a low-noise analog signal procesor for readout of gaseous detectors*, CERN-ECP-94-17.
- [37] ATLAS TRT collaboration, E. Abat et al, *The ATLAS TRT electronics*, 2008 JINST **3** P06007.
- [38] N. Ghodbane, X. Pons and O.M. Rohne, *A method to check the connectivity for the ATLAS TRT Detector*, ATLAS-COM-INDET-2005-009.
- [39] Niels Bohr Institute (NBI), Blegdamsvej 17, DK-2100, København, <http://www.nbi.ku.dk/english/>.
- [40] Item “Dead channels” (extracted from FE electronics tests) from ATLAS TRT End Cap passport, <http://pcwetans.web.cern.ch/pcwetans/research/trt/endcap-passport/>.
- [41] M. Deptuch et al., *Gas Gain Stabilisation System prototype for the TRT*, CERN-ATL-INDET-2002-010.
- [42] Fluorinert, is the trademarked brand name for the line of electronics coolant liquids sold commercially by 3M, <http://en.wikipedia.org/wiki/Fluorinert>.
- [43] H. Danielsson, C. Hauviller, H. Ogren, M. Price, M. Stavrianakou and T. Akesson, *Cooling of the Straws in the ATLAS TRT*, ATL-INDET-95-82.
- [44] J. Grognuz, *ATLAS Transition Radiation Tracker CO₂ cooling system development and validation*, ATL-COM-INDET-2007-009.
- [45] J. Godlewski et al., *Inner Detector Thermal Management and Environmental Gas*, CERN EDMS ATL-IC-EN-0009.
- [46] G. Sprachmann, *Aging and Gas Filtration Studies in the ATLAS Transition Radiation Tracker*, CERN-THESIS-2007-005.
- [47] J. Grognuz, *Manifold optimization for the ATLAS Transistion Radiation Tracker CO₂ cooling system*, technical note, ATL-INDET-2004-004.
- [48] PVSS (Prozessvisualisierungs und Steuerungs-System) is object-oriented process visualization and control system, <http://itcobe.web.cern.ch/itcobe/Services/Pvss/>.